Halide Double Perovskites $Cs_4CuSb_2Cl_{12}$ and $Cs_2AgSbCl_6$: Synthesis and Photocatalytic Application

ASHITHA P P

(MS15026)

A dissertation submitted for the partial fulfilment of

BS-MS dual degree in Science

Indian Institute of Science Education and Research Mohali

June 2020

Certificate of Examination

This is to certify that the dissertation titled "**Halide Double Perovskites Cs$_4$CuSb$_2$Cl$_{12}$ and Cs$_2$AgSbCl$_6$: Synthesis and Photocatalytic Application**" submitted by **Ms. Ashitha P P (Reg. No. MS15026)** for the partial fulfilment of BS-MS dual degree programme of the Institute, has been examined by the thesis committee duly appointed by the Institute. The committee finds the work done by the candidate satisfactory and recommends that the report be accepted.

Dr. Angshuman Roy Choudhury　　　　**Dr. Ujjal K Gautam**　　　　**Dr. Debrina Jana**

(Supervisor)

Dated: June 15, 2020

Declaration

The work presented in this dissertation has been carried out by me under the guidance of Dr. Debrina Jana at the Indian Institute of Science Education and Research Mohali. This work has not been submitted in part or in full for a degree, a diploma, or a fellowship to any other university or institute. Whenever contributions of others are involved, every effort is made to indicate this clearly, with due acknowledgement of collaborative research and discussions. This thesis is a bonafide record of original work done by me and all sources listed within have been detailed in the bibliography.

<div align="right">

Ashitha P P

(Candidate)

Dated: June 15, 2020

</div>

In my capacity as the supervisor of the candidate's project work, I certify that the above statements by the candidate are true to the best of my knowledge.

<div align="right">

Dr. Debrina Jana

(Supervisor)

</div>

Acknowledgement

Ashitha P P

List of Figures

List of Tables

Notations and Abbreviations

AFM	Atomic Force Microscopy
CB	Conduction Band
DSC	Differential Scanning Calorimetry
EDX	Energy-Dispersive X-ray Spectroscopy
FESEM	Field Emission Scanning Electron Microscopy
FTIR	Fourier-Transform Infrared Spectroscopy
HAADF	High-Angle Annular Dark Field Imaging
HRTEM	High-Resolution Transmission Electron Microscopy
MB	Methylene Blue
MCs	Microcrystals
NCs	Nanocrystals
PCE	Photoconversion Efficiency
PLQY	Photoluminescence Quantum Yield
PXRD	Powder X-ray Diffraction
SAED	Selected Area Electron Diffraction
STEM	Scanning Electron Microscopy
TEM	Transmission Electron Microscopy
TGA	Thermogravimetric Analysis
UV	Ultraviolet
VB	Valence Band
XPS	X-ray Photoelectron Spectroscopy

Contents

Abstract

Perovskite nanocrystals (NCs) have gained substantial attention due to their defect tolerant nature, high absorption coefficient, and good charge carrier mobility making them suitable for photovoltaic and optoelectronic applications. For the past few years, lead halide-based perovskites have been developed and achieved excellent electrical and optical properties, but the stability and toxicity issues led to the search for alternative materials. For this, lead-free halide double perovskites became promising due to their higher stability and less toxicity, hence the properties of such materials have been well studied for potential applications. In this thesis, the synthesis and characterization of 2D layered $Cs_4CuSb_2Cl_{12}$ NCs through a facile hot injection synthetic method has been described. The chemical and structural characterizations have been carried out using UV-Vis spectroscopy, PXRD, AFM, TEM, and EDX, and the thermal properties were studied using TGA and DSC. The synthesized NCs are found to be phase pure and have good thermal and moisture stability with narrow bandgap suitable for solar cell applications.

Apart from photovoltaics and optoelectronics, the high stability and bandgap tunability allow perovskite materials to work effectively in photocatalysis under sunlight. Since lead halide perovskites have been ruled out from many applications due to its toxicity, a variety of halide double perovskite materials have been investigating for potential applications but their exploration in photocatalysis is rare. Thus, in this work, the photocatalytic properties of $Cs_2AgSbCl_6$ and $Cs_2Ag_xCu_{(1-x)}SbCl_6$ (x = 0.25, 0.5, 0.75) intermediates have been examined through the photodegradation reaction of MB dye. The photocatalysts were synthesized *via* acid-mediated solution-phase synthetic route. The results show that $Cs_2AgSbCl_6$ exhibits good stability and photocatalytic activity hence can be used as an efficient photocatalyst for dye degradation but a poor degradation rate has been shown by the intermediates.

Chapter 1

Introduction

1.1 Perovskites

Perovskites are compounds having a general formula ABX_3 where A and B are different cations (mono-, di- or trivalent) with same or different oxidation states, and X is an anion (mono- or divalent). The structure consists of corner-sharing BX_6 octahedra with the A cations surrounded by eight such octahedra occupied at the cuboctahedral voids to form three-dimensional (3D) networks.[1,2] An ideal perovskite possesses a cubic structure with a $Pm\bar{3}m$ space group but the structure may be distorted due to the difference in the sizes of the cations to form different crystal structures such as hexagonal or orthorhombic phases which results in unique electronic and optical properties.[3]
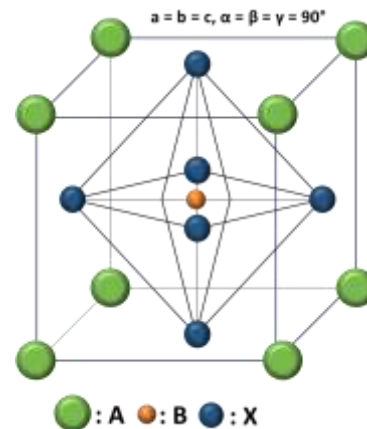
Figure 1. Crystal structure of a typical perovskite of formula ABX_3 (Figure is redrawn from Ref. 4).

The structural stability and formation of the perovskites are predicted using Goldschmidt tolerance factor given by the formula,

$$t = \frac{r_A + r_X}{\sqrt{2\,(r_B + r_X)}}$$

where r_A and r_B are the ionic radii of the ions in the A, B, and X sites.

Typically, the tolerance factor of a stable 3D perovskite structure lies between 0.8 - 1.[4,5] Tolerance factor greater than 1 leads to the formation of structures with lower dimensions. An octahedral factor (μ) defined as $\mu = \frac{r_B}{r_X}$ determines the stability of the BX_6 octahedra and should have a value $\mu > 0.41$ for the formation of perovskites otherwise non-perovskite phases are obtained.[6]

1.2 Properties

Perovskite materials exhibit attractive physical and chemical properties such as superconductivity, ionic conduction characteristics, catalytic properties, thermo-electric, dielectric and optical properties. Halide perovskites possess tunable bandgaps in the visible-near infra-red region with high PLQY. Thus, these materials find their applications in solar cells, sensors, electronic and optical devices.[7]

1.3 Synthetic routes of perovskites

The properties of the perovskite material are dependent on their chemical composition, size, shape, and dimensionality. Hence, these parameters can be tuned by controlling the experimental conditions such as the reaction temperature, time, and precursor concentration. The conventional synthesis of perovskites includes solid-phase synthesis at high temperatures, later several synthetic methods have been developed to improve their properties.[8]

1.3.1 Solid-state method

In solid-state method, stoichiometric amounts of all the precursors are mixed and ball-milled without the use of any solvent. The obtained product is dried and calcined multiple times to achieve single-phase perovskites.

1.3.2 Hydrothermal synthesis

An aqueous solution of the precursors mixed in the stoichiometric ratio is taken into a Teflon-coated hydrothermal autoclave. The solution is treated with high temperature (>200 °C) and pressure for several hours and then cooled to obtain crystalline perovskite powders. The shape and size of the perovskite particles can be controlled by adjusting the reaction temperature, pressure, and pH.[9]

1.3.3 Colloidal synthesis

Colloidal synthesis of perovskites has been developed to obtain high purity NCs and control over the size, shape, and nature of their properties.[10] The major parameters that control the shape and size of the NCs are the precursor concentration, surfactant to precursor ratio, reaction time, and temperature.[11] Solvent induced precipitation, template-assisted method, hot injection and ligand-assisted reprecipitation (LARP) methods became attractive as the reaction is conducted in a liquid phase which is suitable for fabrication processes.[10]

1.3.3.1 Solvent induced precipitation

In this method, the precursor solution containing capping agents and ligands is added to non-polar solvents like acetone at 80 °C to induce the precipitation of the perovskite NCs. The properties of the NCs can be enhanced by adjusting the molar ratios of the precursor.[12]

1.3.3.2 Template-assisted method

In template-assisted synthesis, the precursor solution is deposited on a substrate (or template) coated with a thin oxide film. Kojima *et al.* prepared $MAPbBr_3$ (MA = methylammonium) NCs on a mesoporous TiO_2 layer and later the method has been improved

by depositing the precursors on a gently heat-treated Al_2O_3 layer. Authors have also made MAPbBr$_x$ NCs inside mesoporous silica.[6] Jana and co-workers have developed $CsPbBr_3$ and Mn-doped $CsPbCl_3$ NCs inside mesoporous alumina film to yield pure NCs at room temperature. They could also tune the PL emission inside the film.[13,14]

1.3.3.3 Hot injection method

The hot injection method is often used for the synthesis of metal halide perovskites. This method is based on the sudden injection of a hot solution of one precursor into the remaining hot precursor solution containing solvent and capping agents yielding smaller and monodisperse NCs. This method provides good regulation over the shape and size of the NCs. The drawbacks of this method include the inert reaction condition and limited scalability. Thus, an alternative technique has been developed to overcome these issues.[12]

1.3.3.4 Ligand assisted re-precipitation method (LARP)

In the LARP method, the precursor solution made in a polar solvent is added dropwise to a less polar solvent containing ligands at room temperature. This method is simple and yield crystalline nanoparticles but provides less control over the size and shape of the NCs with poor stability and optical properties.[6,15]

1.3.4 Other synthetic methods

Other synthetic routes include the direct ultrasonic exfoliation and microwave-assisted synthesis. These methods are simple, low-cost, and yield high-quality perovskite NCs. The properties of the NCs can be changed by adjusting the precursor composition and reaction time.[12,16]

1.4 Lead halide perovskites

Oxide perovskites have been vastly investigated for their ferroelectric and dielectric properties but their poor semiconducting properties led to the discovery of metal halide perovskites that exhibit significant improvement in the optical properties and photovoltaic performances.[17,18] Metal halide perovskites show semiconducting properties in terms of ionic and defect tolerant nature that enables the tuning of bandgaps by changing the halide ions to achieve desired optical characteristics.[19,20] Earlier, organic metal halide perovskites had only been studied for their optical properties but later their potential towards solar energy applications was also examined as an alternative for high-cost Si-solar cells. Even though Si-solar cells show excellent efficiency (~30%) and stability, the emergence of solution-processable, scalable and low-cost organic-inorganic hybrid halide perovskites could rapidly increase their PCE from 3.8% to 22.1%.[21,22]

Lead halide perovskites possess distinct photovoltaic and optoelectronic properties owing to their good absorption coefficient, direct bandgaps, high charge carrier mobility, and defect tolerance.[23,24] The VB in a lead halide perovskite is formed by the hybridization of Pb 6s and halide 5p antibonding orbitals whereas the CB is formed from Pb 6p and halide 5p orbitals. These perovskites possess defect tolerance (defect without electronic trap states and doping) due to their electronic band structure forming defect states not in the bandgap but within the VB and CB.[25,26] Such defect tolerant perovskites are highly luminescent and show high PLQY.[27,28]
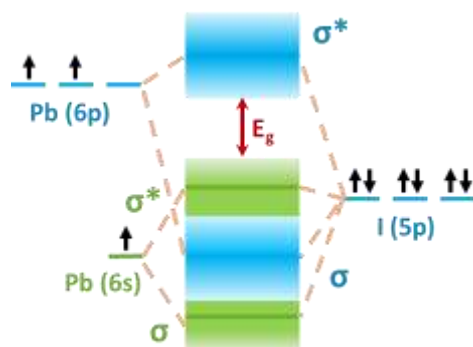
Figure 2. Defect-tolerant band structure of lead halide perovskite (Figure is redrawn from Ref. 19).

Weber developed the first hybrid perovskite, which was a methylammonium (MA)-based lead halide perovskite ($MAPbX_3$ where $X = Cl$, Br, I) and studied its semiconducting properties. After a decade, Mitzi and co-workers did several fabrications on hybrid halide perovskites to obtain an efficient photovoltaic material from them. Tan *et al.* demonstrated $MAPbBr_3$ as a light-emitting material but then Perez–Prieto group synthesized all derivatives of $MAPbX_3$ with exceptionally high PLQY (ratio of emitted photons to absorbed photons) of ~100%.[15] Later Kovalenko and co-workers synthesized purely inorganic $CsPbBr_3$ NCs that yielded highly efficient NC-based LEDs with ~90% of PLQY using low-cost synthetic methods.[24,19]

Though lead halide perovskites have attained a maximum PCE of ~24%, the structural instabilities and degradation occurred by the continuous exposure to heat, light, and moisture made them impractical.[29,30] Several fabrication techniques have been implemented to enhance the stability and performance of lead halide perovskites but the toxicity of lead itself restricted their use from large-scale productions.[31]

1.5 Lead-free halide perovskites

Lead halide perovskites exhibit a high PCE but they become toxic in contact with water and are unstable due to the ionic nature that limits them from various applications.[32,33] To avoid these challenges several approaches have been attempted like substituting Pb^{2+} ions with less toxic divalent cations, in particular, Sn^{2+} and Ge^{2+} from the same group which became inefficient as they readily oxidize and degrade the perovskite material.[34,35] Some theoretical calculations have shown a maximum PCE of ~27% for $MASnI_3$ and $CsGeI_3$ but they could only achieve less than 13% of PCE experimentally.[36]

A heterovalent substitution by replacing Pb^{2+} with trivalent cations like Sb^{3+} and Bi^{3+} having $A_3B_2X_9$ hexagonal structures also led to poor photovoltaic performances with large bandgaps. Park *et al.* reported $MA_3Bi_2I_9$ and $Cs_3Bi_2I_9$ as the first Bi-based double perovskites with a PCE of only 1.09%. Later several researchers employed different synthetic strategies to obtain efficient derivatives of $MA_3Bi_2I_9$ but only $[(CH_3)_3NH]_3Bi_2I_9$ could attain higher thermal and humid stabilities which are promising as light absorbers for solar cells. Walter Rudorff and

Li *et al.* developed Ag and organic cation-based Bi perovskites which showed less than 3% efficiency. Studies on Cs-based Bi halide perovskites revealed that they possess a huge defect in their bandgaps and couldn't use in photovoltaics. Sb-based halide perovskites also showed limited photovoltaic performances due to their defect intolerant nature.[36]

Another mode of heterovalent substitution utilizing a monovalent and a trivalent cation by forming double perovskites became a successful approach in forming stable perovskites.[37,38] Double perovskites have $AB'B''X_6$ formula where A is a monovalent cation, B a divalent cation, and X a monovalent anion in which the BX_6 octahedra is alternatively arranged with B′ and B″ ions at the center.[39] They possess a face-centered structure with an *Fm$\bar{3}$m* space group.[37,40] Lead-free halide double perovskites exhibit similar structure and properties to that of lead halide perovskites but are highly stable under air and water due to the high decomposition enthalpy of their structure.[41] Studies show that Cs-based halide double perovskites with Sb and Bi as trivalent cations along with Cu, Ag, and Au as monovalent cations can form stable perovskites with bandgaps below 2.7 eV which are perfect for optoelectronic applications.[38]
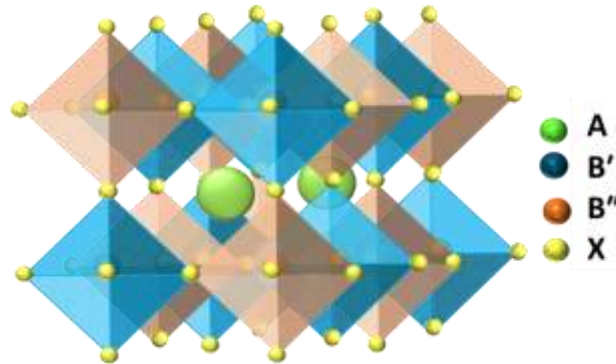
Figure 3. Crystal structure of $AB'B''X_6$ double perovskite (Figure is redrawn from Ref. 39).

Cs-based Bi halide double perovskites such as Cs_2BiAgX_6 and MA_2BiAgX_6 have shown long-term stability with narrow indirect bandgaps but they could reach their efficiency below 10%.[36,42] Li *et al.* reported $MA_2SbAgBr_6$ showing a narrow optical bandgap with high stability have been accepted as a solar cell absorber.[43] In-based double perovskite $Cs_2InBiCl_6$ was also developed but the instability of the perovskite as a result of the oxidation of In made it unfavorable for practical applications whereas $Cs_2AgInCl_6$ shows poor absorption coefficient which is not ideal for solar cell applications.[32,34] Few other double perovskites such as

$Cs_2AgSbCl_6$ and MA_2AgSbI_6 showed good thermal stabilities and Cs_2NaBX_6 (B=Sb, Bi) showed good optical properties and thus can be used in solar devices. Until now, the bandgaps of all the double perovskites reported are too broad for single-junction solar cells.[34,37]

Lead-free halide double perovskites possess low bandgaps, high thermal, and moisture stability useful for photovoltaic applications. But in most halide double perovskites, synthesizing their iodide counterpart in bulk gives unstable phases and hence adopted anion exchange method to achieve them at the nanoscale.[32,44] They exhibit both direct and indirect bandgaps but as the perovskites with indirect bandgaps are not acceptable for optoelectronic applications, several fabrication techniques have been developed to transform indirect bandgaps to direct by altering the pressure, temperature, and doping with a different element.[45] Currently, they are studied for their applications in the field of photocatalysis and water splitting.

1.6 2D layered double perovskites

2D perovskites have emerged as a strategy to deal with the long-term stability of 3D perovskites. According to Goldschmidt's tolerance factor, a value of t > 1 leads to the formation of lower-dimensional derivatives like two-dimensional (2D), one-dimensional (1D), and even zero-dimensional (0D) perovskites from the corresponding 3D structures. Recently 2D layered perovskites showing larger bandgaps, high absorption, and distinct luminescent properties are been widely explored.[46] By changing the size and nature of the 3D ABX_3 structure, 2D layered perovskites of different phases such as Ruddlesden-Popper and Dion-Jacobson are obtained.[35]

Small A cations including Cs and MA generally form 3D structures however several low-dimensional perovskites have been reported with large cations like trimethylammonium and butylammonium. Transition metal-based perovskites have been explored since the last decade due to their electronic and magnetic properties but metals such as Cu, Fe, and Pd form low-dimensional perovskite structures due to their smaller ionic radii compared to Pb.[35] 2D layered structures are formed from metal-deficient perovskites with trivalent metal systems. Such structures are occupied by only two-third of B-site cations such that the remaining sites are vacant which results in metal-deficient layers. In a 2D organic-inorganic hybrid perovskite,

each inorganic layer acts as a potential well and organic component as a potential barrier creating distinct quantum wells in which an increased number in the perovskite layer causes a decrease in the bandgap due to the quantum confinement effect.[47,48] This quantum well structure holds the electrons and holes in the layer. Van der Waal's and hydrophobic interactions between the layers improves the stability of such layered perovskites.[49] Optical properties of these layered perovskites can be tuned by varying the layer number, thickness, and spacing between the layers.[1,12]

Solution processable 2D halide double perovskites can be synthesized by dissolving metal precursors in hydrohalic acid and then precipitating the desired crystals by adding the bulky cation.[1] Another method of synthesis is by grinding the precursors with hydrohalic acid using a mortar and a pestle.[47] Cao *et al.* developed $(BA)_2(MA)_{n-1}Sn_nI_{3n+1}$ perovskite which has shown improved electrical properties and stability than its 3D counterpart $MASnI_3$. Many transition metal-based 2D perovskites showing good magnetic properties were also examined but they all showed poor photovoltaic performances.[34]
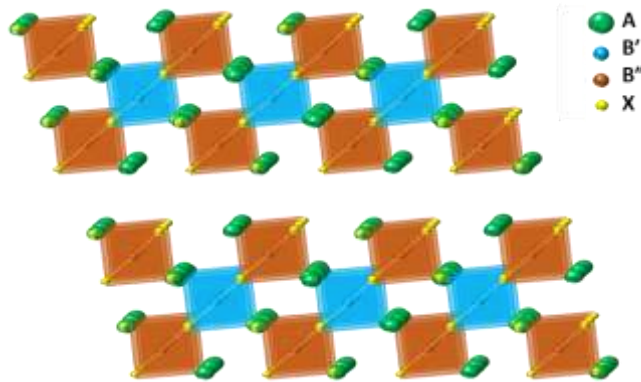
Figure 4. Crystal structure of 2D layered $A_4B'B_2''X_{12}$ double perovskite (Figure is redrawn from Ref. 73).

Sb and Bi-based perovskites mostly show low-dimensional structures yet their properties have not been studied in detail. Both Sb and Bi-based perovskites show structural diversity ranging from 0D to 2D and 3D structures with tunable bandgaps in which their study in photovoltaics started progressing rapidly. 2D perovskites such as $K_3Bi_2I_9$, $Cs_3Bi_2I_9$, and $(NH_4)_3Bi_2I_9$ having unique optical properties were reported but with poor efficiency.[43,50] 1D $Cs_3Sb_2X_9$ (X = Cl, Br, I) nanowires have shown enhanced stability through a colloidal synthetic

method and are found to have fast photo-responsive properties suitable for optoelectronics.[51] Butylammonium (BA) derivatives of $Cs_2AgBiBr_6$ such as $(BA)_4AgBiBr_8$ and $(BA)_2CsAgBiBr_7$ are found to have a 2D structure but they show very weak absorption compared to their 3D counterpart even though they possess a direct bandgap. The band structures obtained from theoretical calculations of these low-dimensional derivatives also revealed that a transition from indirect to direct bandgap can be achieved through dimensional reduction.[46]

In all lead-free perovskites, the idea of electronic dimensionality is important. A good solar cell absorbing material should possess a higher electronic dimensionality. Tang *et al.* designed $Cs_{3+n}M(II)_nSb_2X_{9+3n}$ (M = Sn, Ge) which exhibited good photovoltaic performance. The electronic structure of many low-dimensional perovskites has shown a narrow direct bandgap promising for single-junction solar cells. Some perovskites having 3D structures exhibit electronically 0D and even show large and indirect bandgaps. Zhao *et al.* reported that it is not necessary to obtain a higher electronic dimension from perovskites with a higher structural dimension, however, high electronic dimensionality are favored to attain high-performance photovoltaic materials.[34] Many 2D perovskites show extremely good thermal stabilities, however, the maximum PCE reported for 2D perovskite is only 15.3% which is far lower compared to their 3D counterparts.[34] This motivates us to develop new classes of 2D perovskites that address both stability and performance issues.

1.7 Perovskites in photocatalysis

The development of numerous industries caused severe environmental problems because of the organic dyes present in the waste-water.[52] The degradation of such toxic dyes is important not only to reduce environmental pollution but also to save human health. Photocatalysis has been considered as an effective way to degrade these toxic dyes as the use of solar energy itself minimizes the current global energy demand.[53] The photocatalytic materials used in these reactions are of another concern such that they should be non-toxic and photostable that absorbs light in the UV-vis region. Semiconductor photocatalysis has gained enormous attention due to the unique properties of semiconductors including high absorbance and bandgap tunability. The photoexcitation will occur only if the energy of the absorbed photon is equal to or greater than the bandgap of the semiconducting material.

When a semiconducting catalytic material is irradiated by light, photoexcitation of electrons and holes takes place. The electrons ($\bar{e}$) and holes (h^+) generated lie in the CB and VB respectively, separated by the bandgap. These photogenerated electrons ($\bar{e}$) convert the surface adsorbed oxygen to $\dot{O}_2^-$, and holes (h^+) convert the water (H_2O/OH^-) molecules to $\dot{O}H$. These free radicals initiate the dye degradation.

The general mechanism for a photocatalytic reaction is shown below.[54,55]

$$\text{Photocatalyst} + hv \rightarrow \bar{e} + h^+$$

$$h^+ + H_2O \rightarrow \dot{O}H + H^+$$

$$\bar{e} + O_2 \rightarrow \dot{O}_2^-$$

$$\dot{O}_2^- + H^+ \rightarrow H\dot{O}_2$$

$$2H\dot{O}_2 \rightarrow H_2O_2 + O_2$$

$$H_2O_2 + \bar{e} \rightarrow \dot{O}H + OH^-$$

$$\dot{O}_2^- + \text{substrate} \rightarrow \text{product}$$

$$\dot{O}H + \text{substrate} \rightarrow \text{product}$$

$$\bar{e} + \dot{O}H \rightarrow OH^-$$
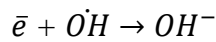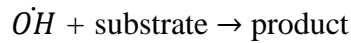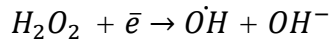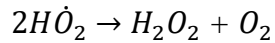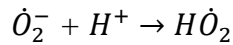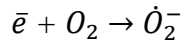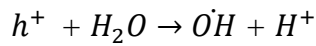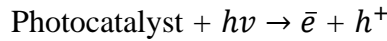
A direct pathway for the degradation of dyes has also been proposed.[55] In this case, the dye molecule (Dye) gets excited from the ground state to the triplet state (Dye*) under visible light. This excited dye molecule is transformed into a radical cation (Dye$^+$) by releasing an electron to the CB of the photocatalyst.

$$\text{Dye} + hv \rightarrow \text{Dye*}$$

$$\text{Dye*} + \text{Photocatalyst} \rightarrow \text{Dye}^+$$
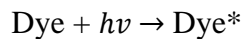
These electrons are reacted with the dissolved oxygen to form $\dot{O}_2^-$ and it further converts to $\dot{O}H$ to undergo dye degradation. Though few reports show a direct mechanism,[56] many reports show that an indirect mechanism is generally followed by most of the catalysts.

$$(2\dot{O}_2^- + 2H^+ \rightarrow 2H\dot{O}_2 \rightarrow H_2O_2 \rightarrow 2\dot{O}H)$$
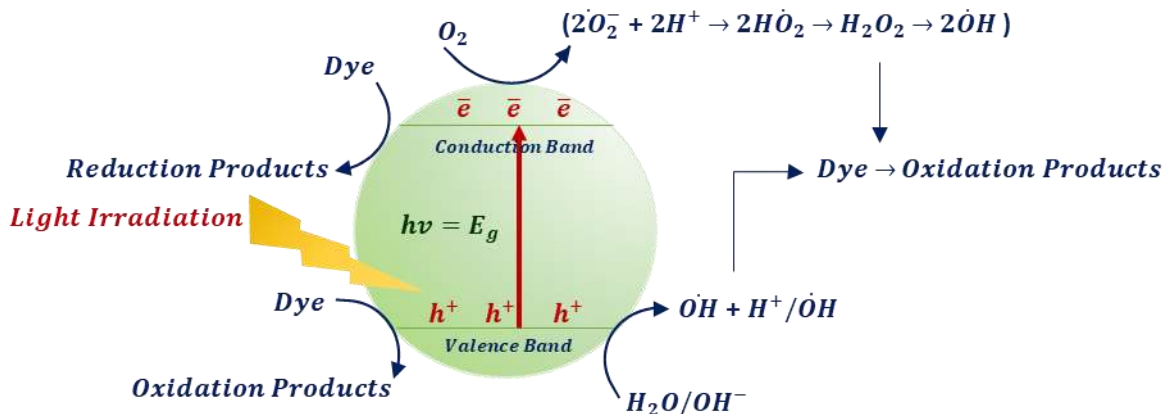
Figure 5. Schematic diagram for the indirect mechanism of dye degradation (Figure is redrawn from Ref. 55).

Photocatalysts such as TiO_2, SnO_2, CdS, and ZnO showing good conversion efficiencies were commonly used in photodegradation and mineralization reactions but they hold a wide bandgap (~3.2 eV) that only absorbs the UV light which limited them from photochemical applications. Thus, the development of photocatalysts showing visible light absorption became necessary. Visible light-driven semiconducting materials such as Fe_2O_3 and Cu_2O were developed but their poor stability and fast recombination of electrons and holes led to the search for new effective materials utilizing solar energy.[57,58] Several approaches such as creating new valence bands and electronic levels between VB and CB through doping have been carried out but the poor stability of such doped materials again made researchers find alternative ways to develop both stable and high-performance photocatalysts.

Perovskites possess stable structures that can be utilized as photocatalysts for various reactions such as carbon dioxide reduction and water splitting; degradation of organic dyes and pollutants; and for different organic syntheses. Apart from their chemical stability, they exhibit long charge-carrier lifetime, optical properties, and tunable bandgaps suitable for photocatalysis. Simple perovskites like titanate and ferrite-based oxide perovskites have been implemented as a cost-efficient photocatalyst for artificial photosynthesis but they work only under UV light because of their large bandgaps (> 3 eV).[59,60] $CaTiO_3$ is one of the perovskite minerals with a bandgap of 3.6 eV and was reported for the photocatalytic water splitting.[59] $BaBiO_3$ perovskite with a small bandgap of 2.0 eV has been examined as a photocatalyst in

photoelectrochemical reaction. Rh-doped $SrTiO_3$ has also been revealed to be a promising photocatalyst for H_2 evolution under visible light.[61,56] The ferro- and piezoelectric properties of the perovskites are also been utilized for the improvement of photocatalytic performance. Alkali-based Nb and Ta perovskites of AMO_3 (A = Li, Na, and K; M = Nb and Ta) kinds exhibited good performance (>55% efficiency for $KNbO_3$) for ferroelectric photocatalytic devices.[62] Later lead halide perovskites such as $CsPbBr_3$ have shown good photocatalytic properties in CO_2 reduction reaction with more than 99% selectivity. Lead-halide perovskites have also shown good photocatalytic activity for organic reactions including α-alkylation of aldehydes.[63,64] But the toxicity of lead restricted its practical use.[65]

Double perovskites, due to the presence of different cations in the B site that generates low bandgap are found to be efficient in visible-light-driven photocatalysis. These structures show improved chemical stability under different catalytic conditions such as high reducing or oxidizing and acidic or basic environments showing good photocatalytic performance. Sr_2FeNbO_6, La_2FeTiO_6, and $CaCu_3Ti_4O_{12}$ double perovskites showing a good photocatalytic activity for hydrogen evolution and degradation of *p*-chlorophenol were reported earlier.[59] After numerous research-works, $Cs_2AgBiBr_6$ has shown excellent performance with suitable bandgap, high stability, and selectivity towards CO_2 reduction. $Cs_2AgBiBr_6$ has recently been studied for its use in photodegradation of dyes.[65,66] Moreover, the structural tuning of the double perovskites through doping affects the catalytic properties enormously and can develop a more successful photocatalyst.

Many low-dimensional perovskites also show superior stability and are known to have a larger surface to bulk ratio than their corresponding 3D derivatives which is suitable for catalysis[67] however most of them have large bandgaps and low charge carrier mobilities making them undesirable for such applications.[68] Since many 2D perovskites have been developed lately with low bandgaps, they are been studied for their potential towards photocatalysis.

1.8 Current Work

Lead-free halide perovskites are of increased interest due to their small bandgaps leading to broader absorption in the visible region giving excellent optoelectronic properties.[15] Many of the lead-free double perovskites have shown good thermal and moisture stability yet their photovoltaic performances are not satisfactory. High-throughput computational studies utilizing density functional theory (DFT) and local density approximation (LDA) calculations predicted the stability of possible lead-free halide perovskites but the experimental outputs of a few of them are still inconclusive.[69,70]

The objective of this work was to synthesize 3D $Cs_2CuSbCl_6$ double perovskite since no successful synthesis of Cu-based double perovskites has been reported yet. Theoretical studies have shown that $Cs_2CuSbCl_6$ has a bandgap of 1.9 eV, which is smaller than the Ag derivative that can exhibit favorable optical properties for single-junction solar cells. The synthesis of $Cs_2CuSbCl_6$ NCs was attempted *via* a bottom-up approach employing a hot injection method, but instead of 3D structure, a 2D layered $Cs_4CuSb_2Cl_{12}$ double perovskite was obtained. Theoretical studies revealed that the decomposition energy of Cu-based double perovskites is comparatively lower than that of the corresponding Ag-based perovskites and hence the stability of $Cs_2CuSbCl_6$ is expected to be lower. Xiao *et al.* reported that the instability of this compound could be attributed to the formation of Cu^+ tetrahedra with halide ions to form a 2D layered structure.[70,71] As many 2D perovskites have shown good optoelectronic properties, detailed characteristics of the obtained $Cs_4CuSb_2Cl_{12}$ NCs were investigated for studying their potential applications.

Perovskite materials have been extensively used in different applications ranging from solar cells to photocatalysis. The second work aims the utilization of $Cs_2AgSbCl_6$ double perovskite in photocatalytic dye degradation. Since the bandgap of a semiconducting material plays a significant role in the photocatalytic activity, $Cs_2AgSbCl_6$ double perovskite having bandgap value 2.53 eV (which is lower than the energy of visible light) is expected to show good photocatalytic performance. In this work, the photocatalytic activity of $Cs_2AgSbCl_6$ and $Cs_2Ag_xCu_{(1-x)}SbCl_6$ (x = 0.25, 0.5, 0.75) intermediates towards MB dye degradation has been investigated.

1.9 Instrumentation

UV-visible spectra of the NCs dispersed in toluene were measured using Cary 5000 UV-Vis-NIR spectrophotometer (Agilent Technologies) from 280 – 1100 nm range at a scan rate of 1 nm/s. Powder X-ray Diffraction (PXRD) data were recorded on Rigaku Ultima IV diffractometer enabled with Cu Kα (1.54 Å) radiation with a scan rate of 2°/min ranging from 15-60°. Transmission electron microscopic (TEM) studies were done using JEM-F200 (JEOL) with an energy dispersive X-ray scattering (EDX) facility. Field Emission scanning electron microscopy (FESEM) was done using JEOL-7600F. TGA analysis was performed using DTG-60H from Shimadzu with a heating rate of 5 °C/ min up to 1000 °C. DSC analysis was done using Perkin Elmer DSC 8000. Atomic Force Microscopy (AFM) was carried out using Asylum Research Atomic Force Microscope. The height profile of the sample was measured using a scanning probe microscope (NANOSENSORS). X-ray photoelectron spectroscopy (XPS) was done using the Nexsa model of Thermofisher Scientific. FTIR characteristics were examined using Perkin Elmer from 400–4000 cm^{-1}.

Chapter 2

Project 1: Synthesis of 2D layered Cs$_4$CuSb$_2$Cl$_{12}$ double perovskite

A wide variety of 2D hybrid perovskites that possess remarkable properties have been investigated but Sb and Bi-based halide double perovskites are less explored. Cortecchia *et al.* developed MACu$_2$Cl$_x$Br$_{4-x}$ perovskites and examined their properties for photovoltaic applications. These perovskites have shown a propensity to form 2D layered structures because of the small ionic radius of Cu^{2+} ion compared to that of Pb^{2+}ion. Li *et al.* reported another Cu-based perovskite C$_6$H$_4$NH$_2$CuBr$_2$I as a light absorber which resulted in a PCE of only 0.5%. Thus, the generation of high-performance transition metal-based perovskites is still challenging but can be achieved through several fabrication techniques that offer stable and highly efficient photovoltaic materials.[36] Here, we report the synthesis of 2D layered Cs$_4$CuSb$_2$Cl$_{12}$ perovskite NCs *via* a facile hot injection synthetic route for the first time. To date, Cs$_4$CuSb$_2$Cl$_{12}$ MCs have been developed using mechanochemical solid-state synthesis and acid-mediated solution-phase synthesis.[72,73] Single-layered Cs$_4$CuSb$_2$Cl$_{12}$ NCs have been achieved *via* a top-down synthetic procedure employing an ultrasonic exfoliation method but this method has disadvantages such as the use of high-energy and less polar solvents.[49] The synthesized Cs$_4$CuSb$_2$Cl$_{12}$ perovskite NCs show a narrow bandgap of value within 1.3-1.6 eV and can be used as a promising material in photovoltaics.

Experimental Section

2.1 Materials

Cesium carbonate (Cs_2CO_3, 99.9%, Sigma-Aldrich), cesium chloride (CsCl, 99.9%, SRL), cesium bromide (CsBr, 99.9%, Alfa Aesar), copper (I) chloride (CuCl, 99.9%, Sigma-Aldrich), copper (II) chloride ($CuCl_2 \cdot 2H_2O$; 99.9%, Sigma-Aldrich), copper (I) bromide (CuBr, 98%, Sigma-Aldrich), antimony (III) acetate ($Sb(ac)_3$, 99.99%, Sigma-Aldrich), antimony (III) chloride ($SbCl_3$, 99%, SRL), antimony (III) bromide ($SbBr_3$, 99%, Alfa Aesar), diphenyl ether (DPE, 99%, Spectrochem), oleic acid (OA, 99.9%, Sigma-Aldrich), oleylamine (OAm, 99.9%, Sigma-Aldrich), benzoyl chloride (99%, Fisher Scientific), benzyl chloride (97%, Sigma-Aldrich), benzoyl bromide (97%, Sigma-Aldrich), trimethylsilyl chloride (TMSCl, >99%, Sigma-Aldrich), trimethylsilyl bromide (TMSBr, >97%, Sigma-Aldrich), N-Chlorosuccinimide (NCS, 98%, Sigma-Aldrich), hydrochloric acid (HCl, 37%, Merck), hydrobromic acid (HBr, 47%, AVRA).

2.2 Synthetic protocol for $Cs_4CuSb_2Cl_{12}$ double perovskite

2.2.1 Synthesis of 2D $Cs_4CuSb_2Cl_{12}$ NCs *via* hot injection method

The protocol for the synthesis of the NCs was slightly modified from the article reported by Manna et al.[74] The Cs-oleate precursor was prepared by taking 400 mg of Cs_2CO_3 in 2.4 mL of OA and 16 mL of DPE in a Schlenk flask. This mixture was vacuum dried at 120 °C for 1h under vigorous stirring followed by heating to 150 °C under nitrogen atmosphere.[75]

For the synthesis of $Cs_4CuSb_2Cl_{12}$ NCs (DPCl**1**), 0.25 mmol of $CuCl_2 \cdot 2H_2O$ and 0.25 mmol of $Sb(ac)_3$ were dissolved in DPE (1mL), dried OA (1mL), dried Cs-oleate and OAm (1mL) in a 50 mL Schlenk flask. The reaction mixture was vigorously stirred under vacuum at 120 °C for 1h and a nitrogen atmosphere was provided by increasing the temperature to 150 °C. After the temperature reached 150 °C, 1 mL of dried benzoyl chloride-DPE (1:2 ratio, v/v) mixture was quickly injected into the reaction mixture and quenched the reaction by keeping in an ice bath after 10 s. The obtained solution was washed twice with toluene by centrifuging at 8000 rpm for 20 minutes to a obtain brown-colored pellet.

The reaction was also carried out using CuCl as the copper source. For the synthesis of $Cs_4CuSb_2Br_{12}$ (DPBr**1**), a similar procedure was followed with the same precursors except for CuCl and benzoyl chloride. Instead, CuBr and benzoyl bromide were used.
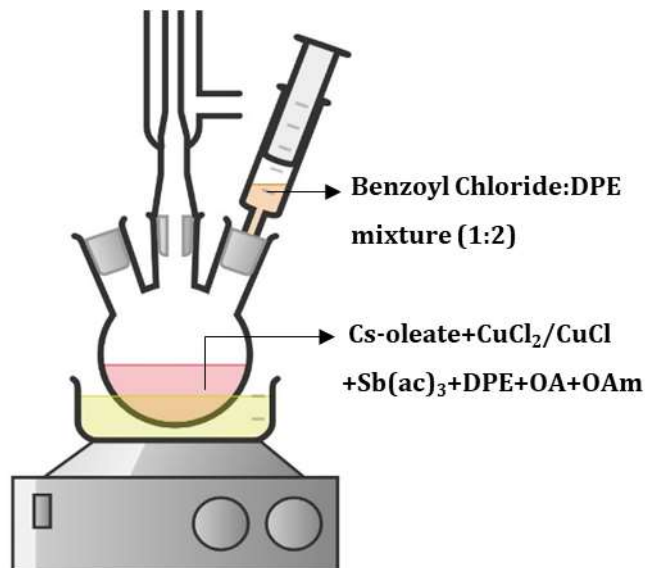
Figure 6. Hot injection synthesis of $Cs_4CuSb_2Cl_{12}$ NCs.

2.2.2 Synthesis of 2D $Cs_4CuSb_2Cl_{12}$ MCs *via* acid-mediated solution-phase route

1 mmol of $SbCl_3$ and 1 mmol CuCl were added to 5 mL conc. HCl (37%) solution. After stirring for 30 minutes, the mixture was heated to 75 °C and 2 mmol of CsCl was added to the reaction mixture and kept for 1h with constant stirring. The precipitate was filtered out and washed with ethanol to get a black powdered $Cs_4CuSb_2Cl_{12}$ MCs (DPCl**2**).[76] The same procedure was followed for the synthesis of $Cs_4CuSb_2Br_{12}$ (DPBr**2**) with $SbBr_3$, CuBr, and CsBr as precursors in conc. HBr (47%) solution.
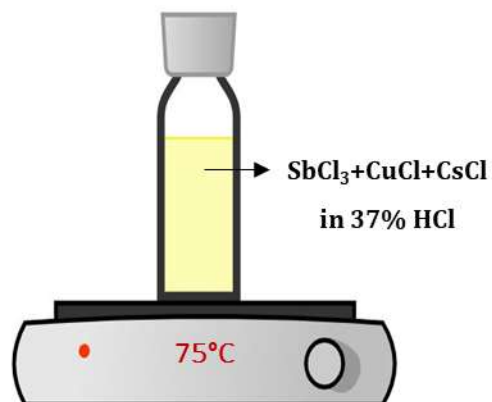
Figure 7. Acid-mediated solution-phase synthesis of $Cs_4CuSb_2Cl_{12}$ MCs.

2.3 Anion exchange reaction

To the synthesized $Cs_4CuSb_2Cl_{12}$ (25 mg) NCs dispersed in toluene, 1 mL TMSBr was added and stirred for 10 minutes.[77] The obtained reddish-brown precipitate (DPBr**3**) was dried for further characterizations.

Results and Discussion

The structural and morphological characterization of the $Cs_4CuSb_2Cl_{12}$ NCs obtained through hot injection method were done using TEM, PXRD, and AFM, and the thermal properties were analyzed using TGA and DSC. For $Cs_4CuSb_2Cl_{12}$ MCs, PXRD and FESEM were carried out.

To understand the crystal structure of the synthesized NCs, powder XRD was carried out. From the data, the obtained $Cs_4CuSb_2Cl_{12}$ NCs (DPCl**1**) are found to be phase pure and matches well with the 2D layered $Cs_4CuSb_2Cl_{12}$ MCs reported earlier. The XRD patterns of the synthesized MCs (DPCl**2**) show a monoclinic $C2/m$ structure. Figure 8 shows the XRD patterns of the synthesized $Cs_4CuSb_2Cl_{12}$ NCs and MCs compared with the JCPDS data.
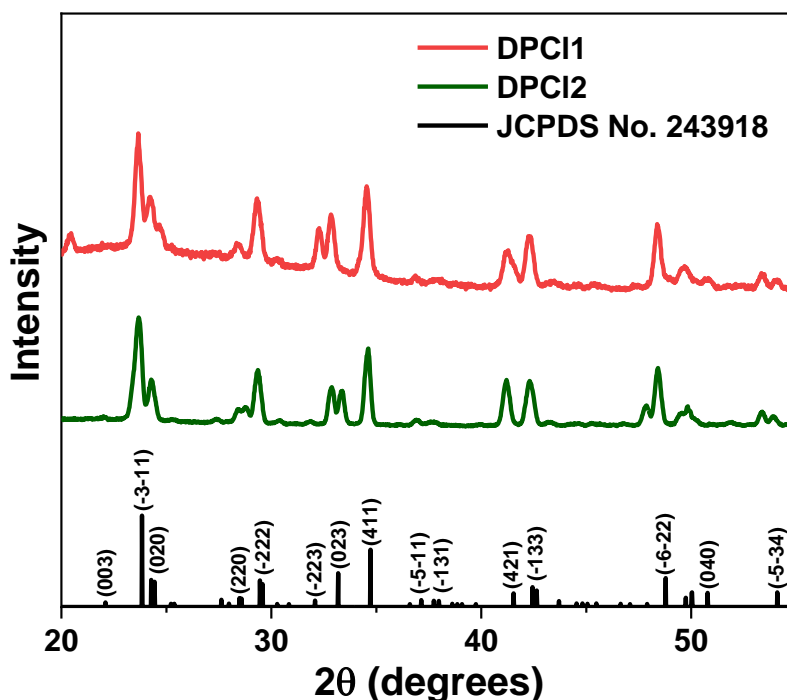
Figure 8. PXRD patterns of DPCl**1** NCs synthesized through hot injection method and DPCl**2** MCs obtained through acid-mediated solution-phase synthetic route.

Figure 9 shows the UV-Vis spectrum of $Cs_4CuSb_2Cl_{12}$ NCs dispersed in toluene. The compound shows an absorption peak around 556 nm and the corresponding Tauc plot gives a narrow bandgap of value between 1.3 to 1.6 eV.
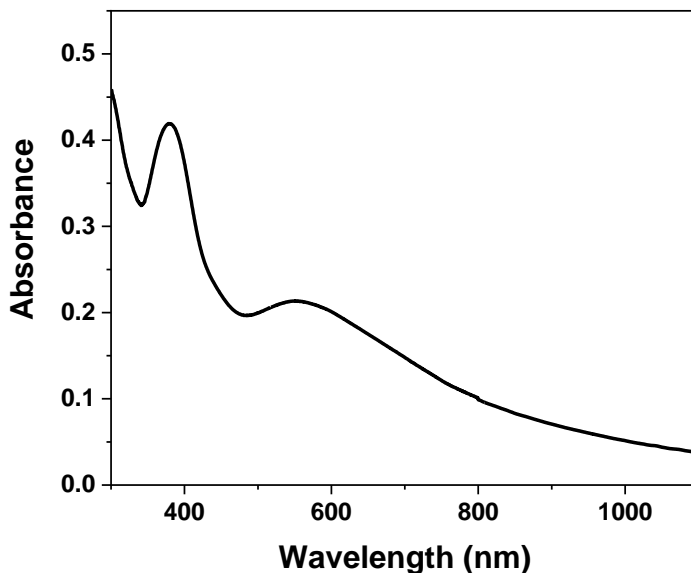
Figure 9. UV-Vis spectrum of $Cs_4CuSb_2Cl_{12}$ NCs.

A scaled-up synthesis of the NCs was also done to check the large-scale productivity showing the same crystal structure evident from the PXRD data (Figure 10).
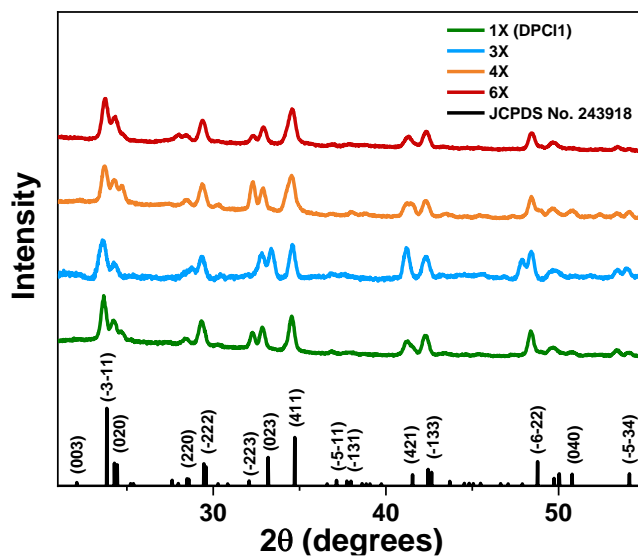
Figure 10. PXRD patterns of the scaled-up products of $Cs_4CuSb_2Cl_{12}$ NCs (DPCl**1**) synthesized through hot injection method.

Cs$_4$CuSb$_2$Cl$_{12}$ MCs were obtained *via* acid-mediated solution-phase synthesis. The FESEM images shown in Figure 11 reveals the formation of octahedral microcrystals. The FESEM images of the product obtained through solution-phase synthesis of the bromide counterpart show microcrystals without any distinguishable crystal phase (Figure 12).
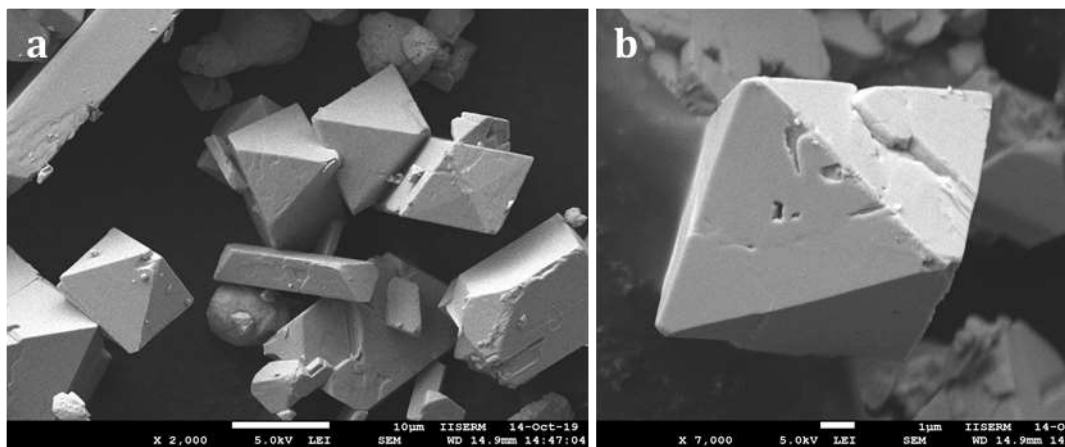
Figure 11. FESEM images of DPCl**2** MCs obtained through acid-mediated solution-phase synthesis at (a) low and (b) high magnification.
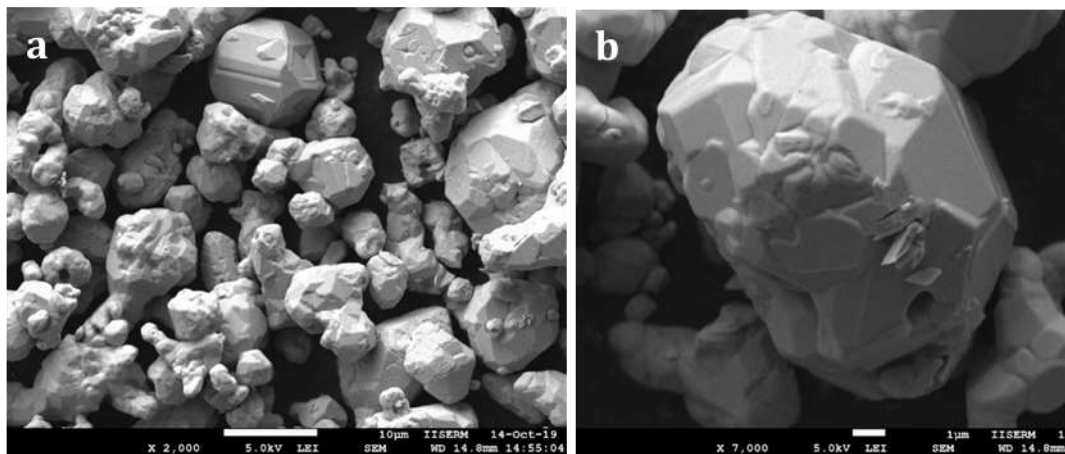
Figure 12. FESEM images of DPBr**2** MCs obtained through acid-mediated solution-phase synthesis at (a) low and (b) high magnification.

To check the suitability of the formation of the NCs, other sources of precursors were also used. CuCl and $SbCl_3$ were used instead of $CuCl_2$ and $Sb(ac)_3$ respectively. The PXRD pattern of the product obtained with CuCl as precursor shows a structure similar to DPCl**1** (Figure 13) whereas due to the hygroscopic nature of $SbCl_3$ an impure crystal structure is observed (Figure 14) due to the formation of SbOCl.
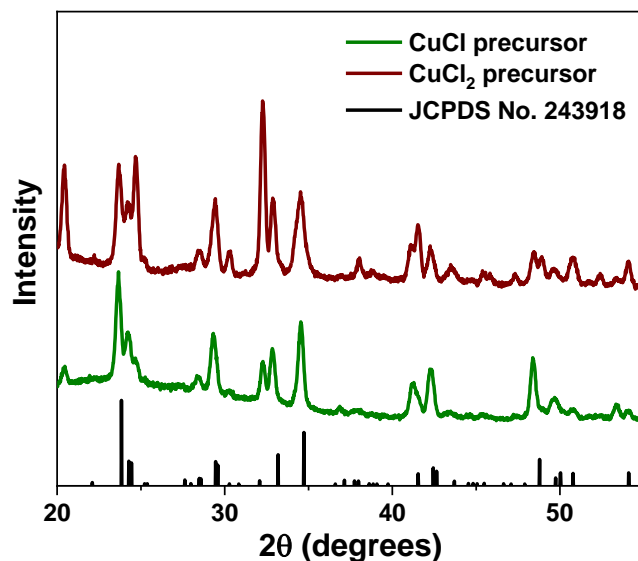
Figure 13. PXRD patterns of the NCs obtained using CuCl and $CuCl_2$ precursors through hot injection method.
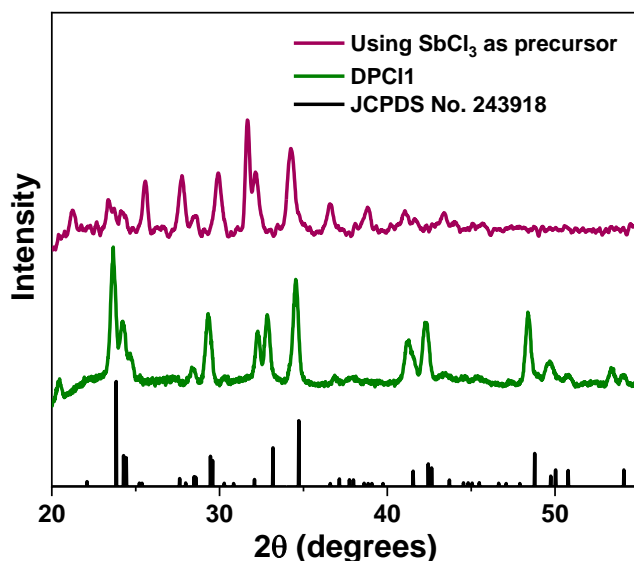
Figure 14. PXRD pattern of the product obtained with $SbCl_3$ as precursor instead of $Sb(ac)_3$ compared with DPCl**1** NCs.

For chloride source, benzoyl chloride was replaced by TMSCl, benzyl chloride, and NCS to examine the product formation. But the reaction with TMSCl only resulted in the product formation (Figure 15) due to its superior chlorination ability compared to other chloride sources chosen. The result of the reactions with different chloride sources is summarized in Table 1.
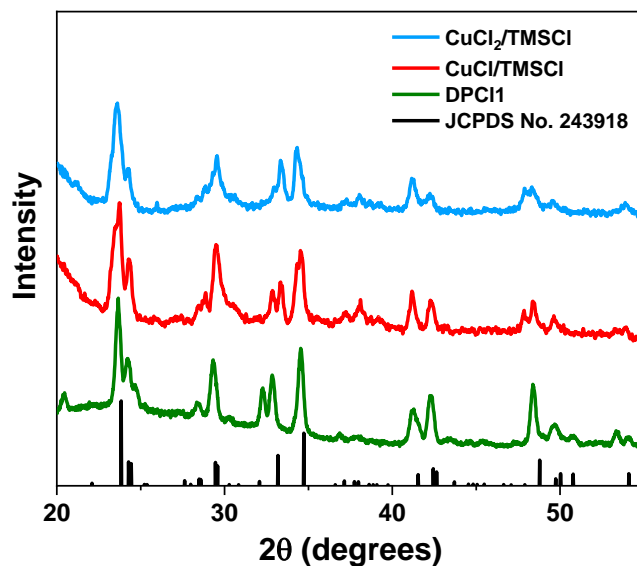
Figure 15. PXRD patterns of the NCs obtained using TMSCl along with CuCl and $CuCl_2$ precursors as copper sources.

Table 1. Synthesis of $Cs_4CuSb_2Cl_{12}$ NCs with different chloride sources.

Chloride source	Copper source	Reaction
Benzoyl chloride	$CuCl/CuCl_2$	Product forms
Benzyl chloride	$CuCl/CuCl_2$	No product formation
TMSCl	$CuCl/CuCl_2$	Product forms
NCS	$CuCl/CuCl_2$	No product formation

Structural morphology and compositional characterization of $Cs_4CuSb_2Cl_{12}$ NCs were done using TEM-EDX analysis. For TEM analysis, $Cs_4CuSb_2Cl_{12}$ NCs dispersed in toluene was drop cast onto the copper-coated Ni grid. From the TEM studies (Figure 16), the particles were found to be spherical with an average size of 3.9 nm.
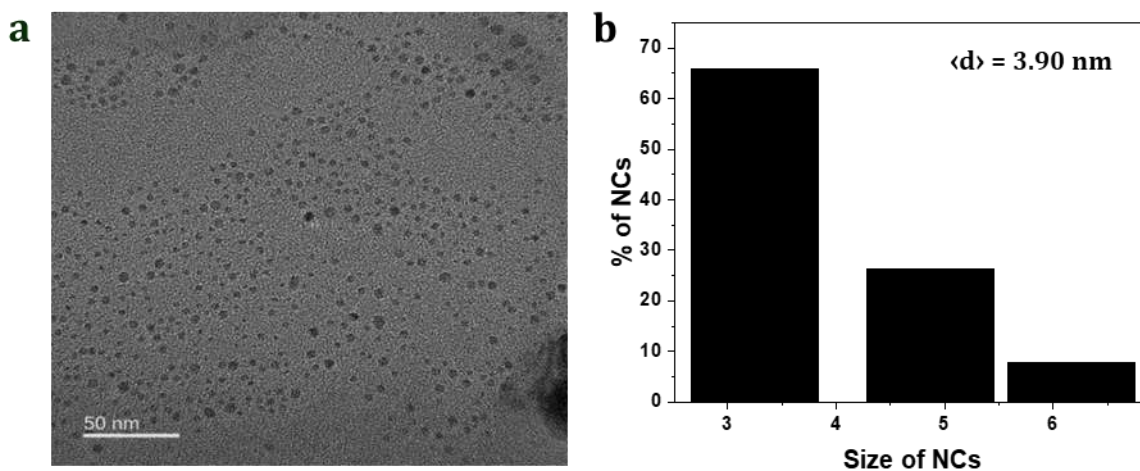
Figure 16. TEM images of $Cs_4CuSb_2Cl_{12}$ NCs showing (a) the particles and their morphology, (b) size distribution of the NCs.

HRTEM images of the NCs show the fringes corresponding to (-133) and (411) planes and SAED pattern shows spots corresponding to different planes from the sample (Figure 17).
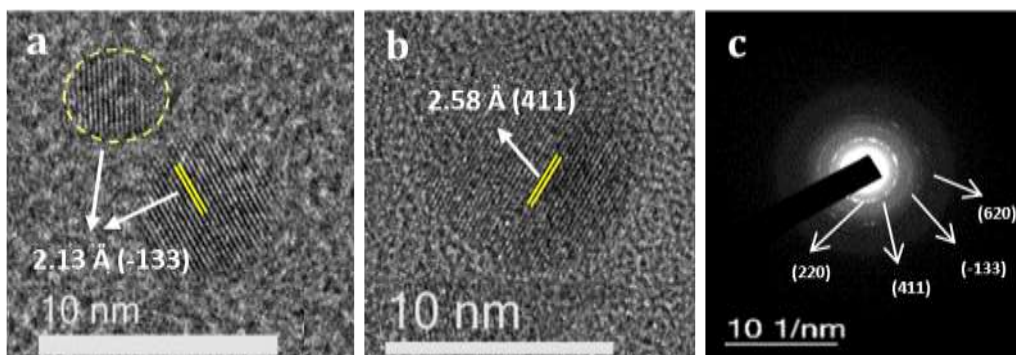
Figure 17. (a, b) HRTEM images of $Cs_4CuSb_2Cl_{12}$ NCs showing fringes corresponding to (-133) and (411) planes. (c) SAED pattern showing the crystalline nature of the NCs.

Figure 18 shows the HAADF-STEM images and the elemental mapping corresponding to each element in the sample indicating the presence of Cu and Sb throughout the region.
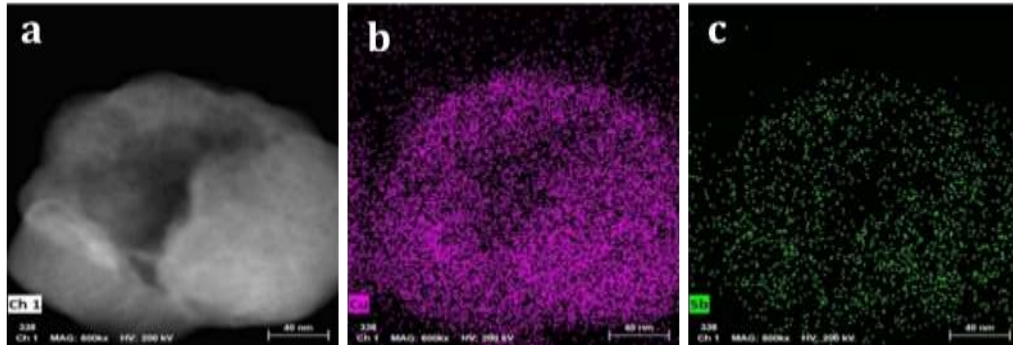
Figure 18. (a) HAADF-STEM image of an agglomerated portion in the TEM grid and their corresponding color mapping showing the presence of Cu and Sb (b and c).

Figure 19 shows the peaks of the elements present in the sample obtained from EDX analysis. Peaks corresponding to the non-constituent elements come from the TEM grid (Ni) and TEM instrument (Au and Zr). The percentage composition obtained from EDX analysis is listed in Table 2.
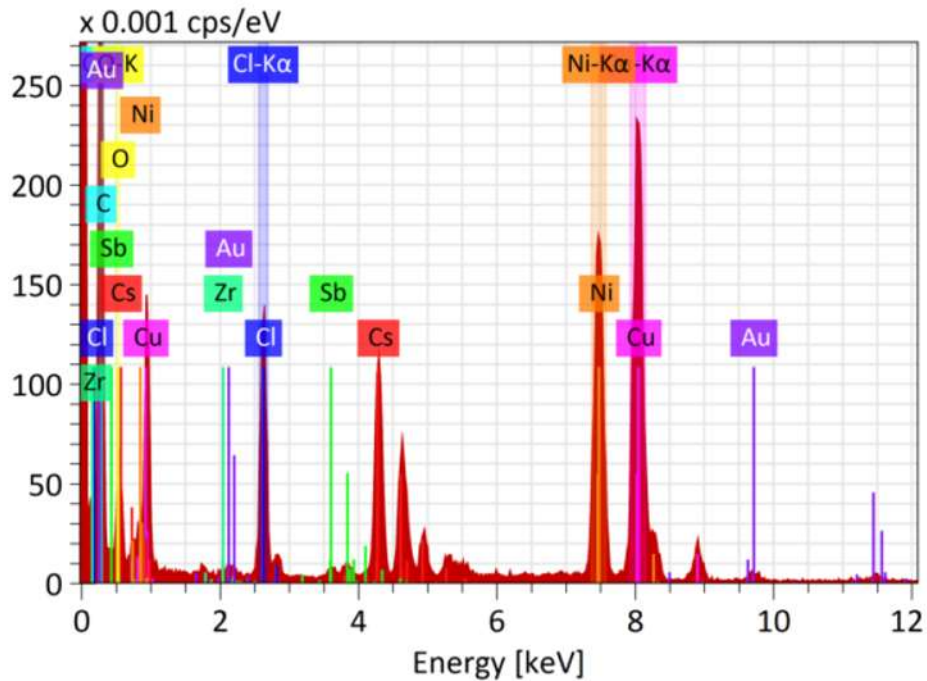
Figure 19. TEM-EDX analysis showing peaks of elements present in the sample.

Table 2. Atomic % ratios of the constituent elements of DPCl**1** obtained from TEM-EDX analysis.

Element	Atomic % ratio
Cs	4.1
Cu	1.2
Sb	2.2

The reaction was also carried out at 180 °C showing particles with spherical morphology but they are found to be agglomerated in TEM images (Figure 20) indicating that the ideal temperature for the reaction is 150 °C.
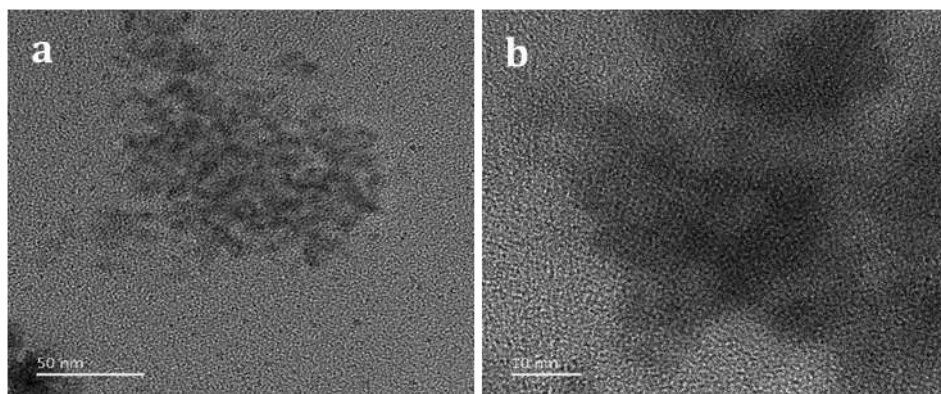
Figure 20. TEM images of $Cs_4CuSb_2Cl_{12}$ NCs prepared at 180 °C showing the agglomeration at (a) low and (b) high magnification.

The oxidation states of the constituent elements present in the NCs were confirmed by XPS. From the XPS data, the presence of Cs (+1), Cu (+2), Sb (+3), and Cl (-1) reveals the formation of $Cs_4CuSb_2Cl_{12}$ NCs (Figure 21).
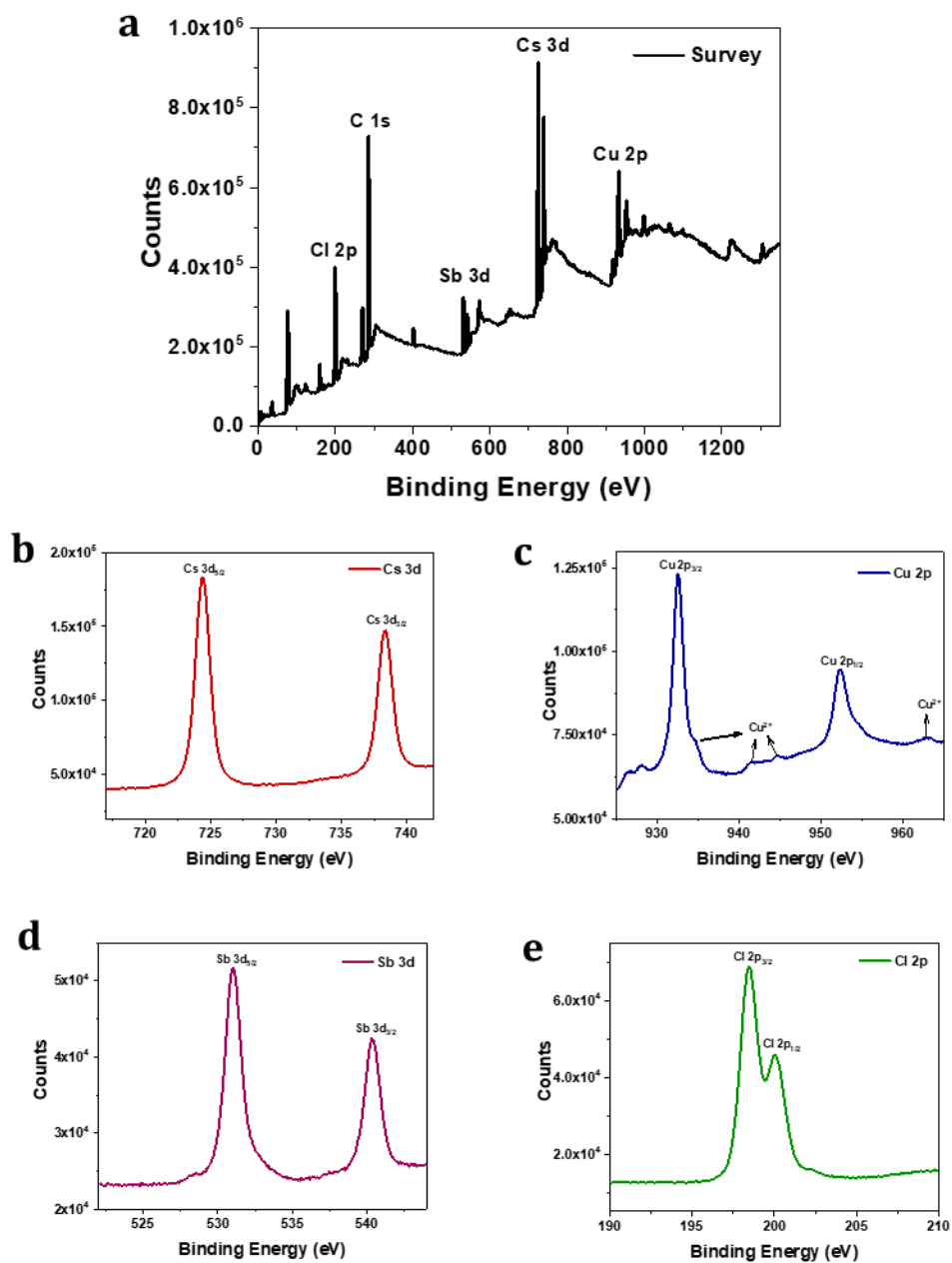
Figure 21. XPS analysis of $Cs_4CuSb_2Cl_{12}$ NCs (a) survey scan (b-e) Cs (3d), Cu (2p), Sb (3d) and Cl (2p).

The thermal characteristics of the NCs were studied using TGA and DSC. TGA was performed from 30 °C to 1000 °C and the weight loss of the sample was monitored. The sample was found to be stable up to 185 °C and after that started losing the weight till 725 °C. The weight loss can be ascribed to the evaporation of organic solvents and ligands at low temperatures and the evaporation of the inorganic part to other compounds at higher temperatures. Figure 22 shows the TGA of the NCs.
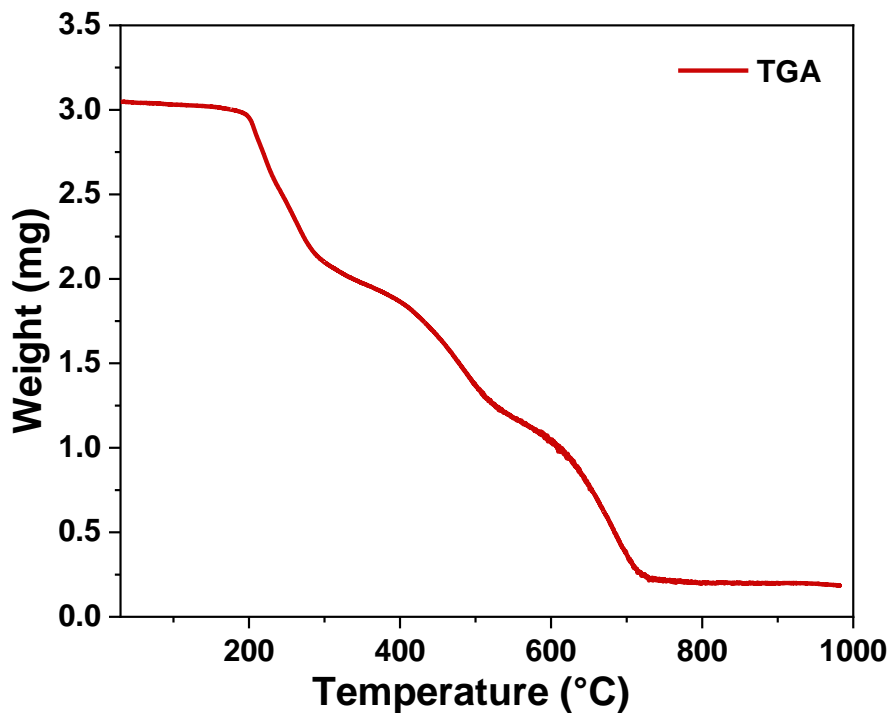
Figure 22. TGA of $Cs_4CuSb_2Cl_{12}$ NCs showing weight loss up to 725 °C.

DSC analysis was done by heating the sample from -10 °C to 210 °C and again cooling back to -10 °C but no phase transitions were observed from room temperature to 180 °C. Figure 23 shows the DSC data of the NCs.
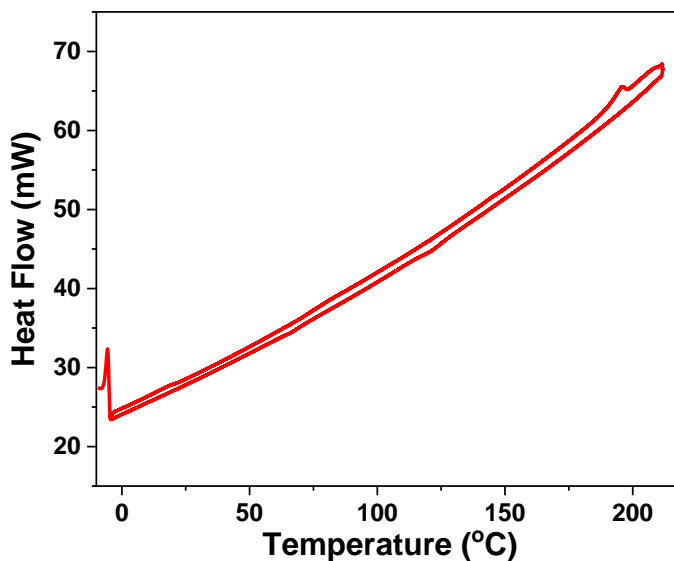
Figure 23. DSC analysis of $Cs_4CuSb_2Cl_{12}$ NCs.

The stability of the NCs was examined under air with an average relative humidity of 74% for 130 days and at 80 °C temperature for 10 days showing no changes in the PXRD patterns (Figure 24) confirming that the samples are highly stable.
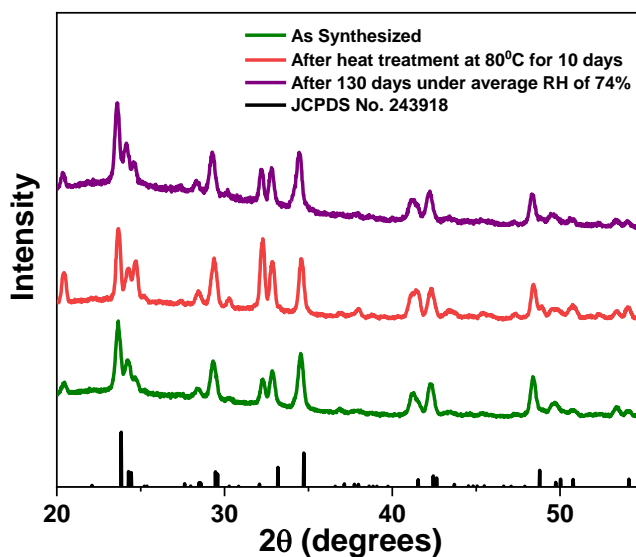
Figure 24. PXRD patterns of $Cs_4CuSb_2Cl_{12}$ NCs under different conditions showing their stability.

The topography and the height of the NCs were obtained from AFM. The cantilever of the microscope was scanned over the surface of the sample showing disc-shaped NCs with an average thickness of ~1 nm corresponding to the length of a single unit cell (Figure 25).
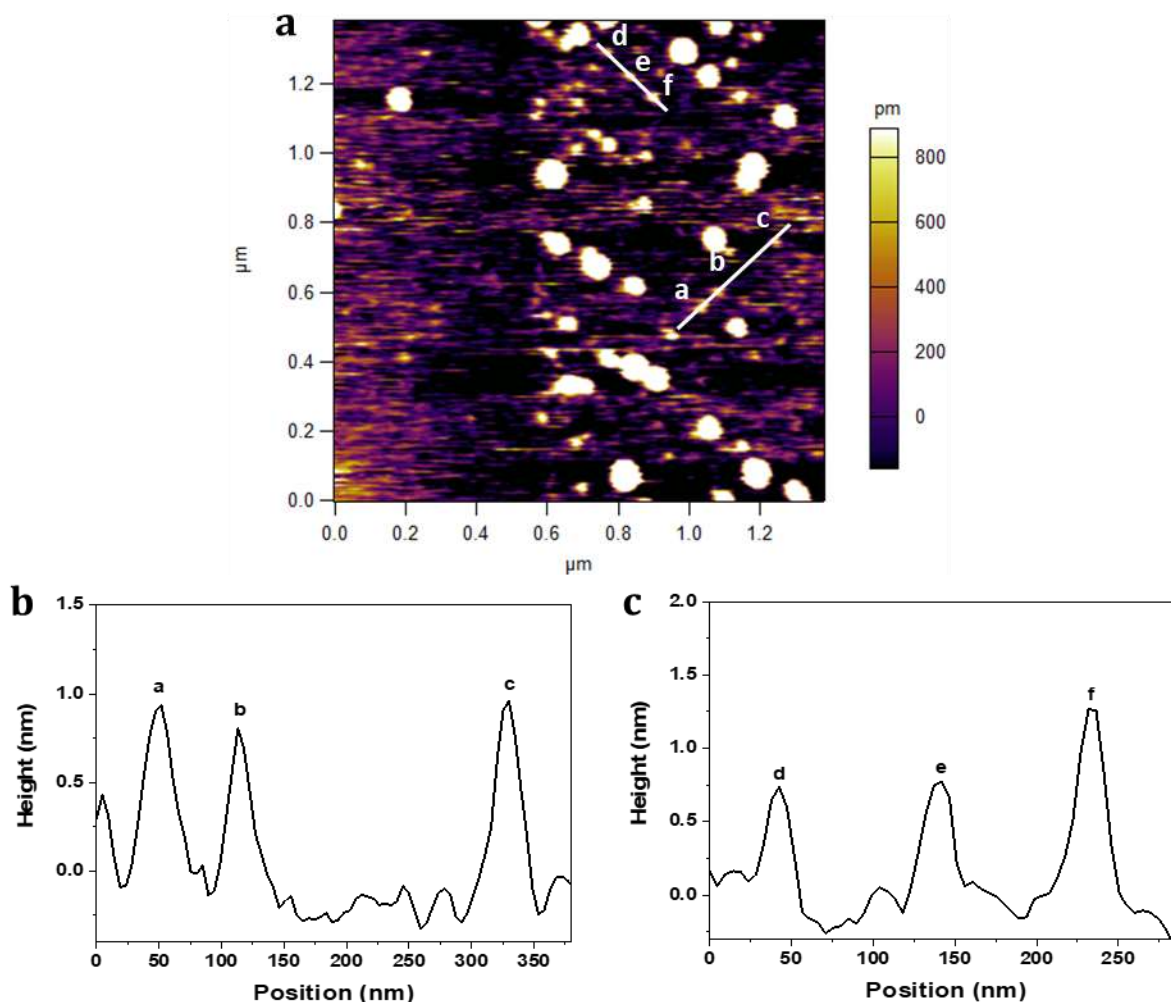
Figure 25. AFM characteristics of $Cs_4CuSb_2Cl_{12}$ NCs showing their topography (a) and height profiles of particles from different regions (b and c).

The synthesis of the bromine analog of the $Cs_4CuSb_2Cl_{12}$ NCs was also carried out through hot injection synthesis, acid-mediated solution-phase synthesis, and anion exchange reaction but the PXRD patterns of the products obtained from these synthetic routes reveal that $Cs_4CuSb_2Br_{12}$ was not formed. Figure 26 shows the PXRD patterns of the obtained products compared with $Cs_4CuSb_2Cl_{12}$ NCs.
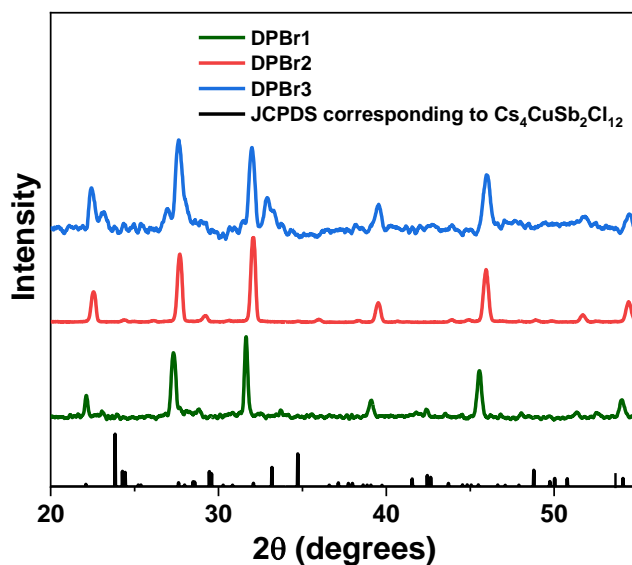
Figure 26. PXRD patterns of the products DPBr**1**, DPBr**2**, and DPBr**3** compared with the JCPDS data of $Cs_4CuSb_2Cl_{12}$.

FTIR characteristics of the $Cs_4CuSb_2Cl_{12}$ NCs with and without heat treatment was analyzed (Figure 27). The peak corresponding to N-H stretch (2924 cm^{-1}), C-H stretch (2853 cm^{-1}), and C-H bend (1579 cm^{-1}) of the organic components (capping ligands and solvent) were significantly diminished after the heat treatment indicating the evaporation of them under heat.
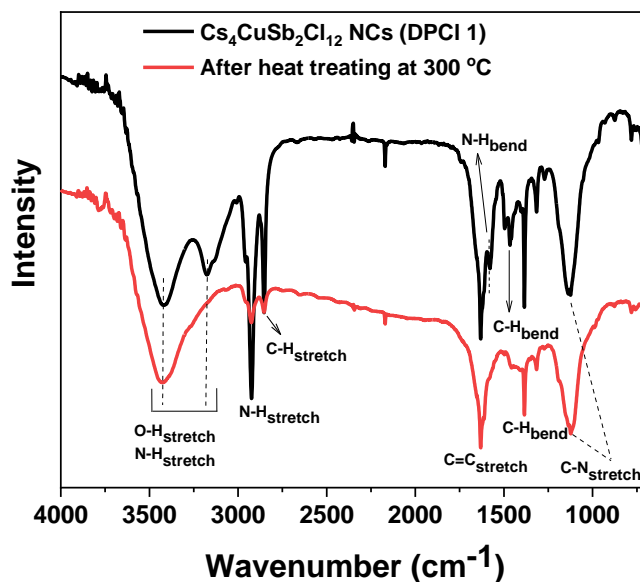
Figure 27. FTIR spectra of $Cs_4CuSb_2Cl_{12}$ NCs before and after heat treatment at 300 °C.

Chapter 3

Project 2: Application of $Cs_2AgSbCl_6$ double perovskite as photocatalyst

Lead halide perovskite has been considered as a promising semiconducting material in solar cells, photodetectors, and photocatalysis because of their tunable bandgaps and high charge-carrier mobility. Many lead halide perovskites like $CsPbX_3$ and $MAPbX_3$ (X = Cl, Br, I) have shown long charge carrier diffusion length leading to good photocatalytic performance.[68,78] Recently, lead-free halide perovskites $Cs_3Bi_2X_9$ (X = Cl, Br, I) and $Cs_2AgBiBr_6$ showing an indirect bandgap, good stability, and long carrier recombination lifetime have been reported as an environment-friendly perovskite photocatalyst for CO_2 reduction and dye degradation.[79,80] To date, only a few lead-free halide perovskites have been reported as photocatalysts and thus, the study of photocatalytic activity of $Cs_2AgSbCl_6$ becomes interesting as no reports are available for this perovskite as a photocatalyst. MB dye is an organic cationic dye used in pharmaceuticals and textile industries as coloring agents. The aromatic amines present in this dye cause harmful effects to the environment and thus, the degradation of this toxic dye becomes necessary.[62] In this work, the degradation kinetics of MB dye using $Cs_2AgSbCl_6$ as photocatalyst has been examined using pseudo-first-order kinetic plots. The photo-degradability of $Cs_2Ag_xCu_{(1-x)}SbCl_6$ (x = 0.25, 0.5, 0.75) intermediates was also evaluated. The degradation reaction was carried out from IISER Mohali.

Experimental Section

3.1 Materials

Cesium chloride (CsCl, 99.9%, SRL), copper (I) chloride (CuCl, 99.9%, Sigma-Aldrich), antimony (III) chloride ($SbCl_3$, 99%, SRL), silver chloride (AgCl, 99.9%, Sigma-Aldrich), hydrochloric acid (HCl, 37%, Merck), methylene blue trihydrate (99%, SRL).

3.2 Synthesis of 3D $Cs_2AgSbCl_6$ MCs for photocatalysis

For the synthesis of $Cs_2AgSbCl_6$ acid-mediated solution-phase synthesis was followed. For this, equimolar amounts (1 mmol) of $SbCl_3$ and AgCl were added to 5 mL conc. HCl (37%) solution and stirred for 30 minutes. 2 mmol of CsCl was added to the reaction mixture and kept for 1h after heating the solution to 75 °C. The filtered-out precipitate was washed with ethanol to get the desired MCs. Stoichiometric amount of Ag and Cu precursors were used for the synthesis of $Cs_2Ag_xCu_{(1-x)}SbCl_6$ (x = 0.25, 0.5, 0.75) intermediates.

3.3 Photocatalytic degradation of MB dye

The photocatalytic activity of 3D $Cs_2AgSbCl_6$ MCs and $Cs_2Ag_xCu_{(1-x)}SbCl_6$ (x = 0.25, 0.5, 0.75) intermediates were examined by observing the photodegradation kinetics of MB dye under sunlight. A stock solution of 1.5 mg of MB dye dissolved in 10 mL of water was initially prepared and then diluted to 35 times. To 10 mL of the diluted stock solution, 20 mg of the photocatalyst was added and kept under sunlight with constant stirring. Different sets of the reaction were kept for different intervals of time (30 min to 4h) and the reaction mixture after removing the photocatalyst was taken for further studies.

Results and Discussion

The structural and morphological characterization of the 3D $Cs_2AgSbCl_6$ and its intermediates have been studied. The PXRD patterns of $Cs_2AgSbCl_6$ and $Cs_2Ag_xCu_{(1-x)}SbCl_6$ (x = 0.25, 0.5, 0.75) intermediates show cubic double perovskite structure with $Fm\overline{3}m$ space group that matches with earlier reports.[81,82] The PXRD pattern of $Cs_2AgSbCl_6$ is shown in Figure 28.
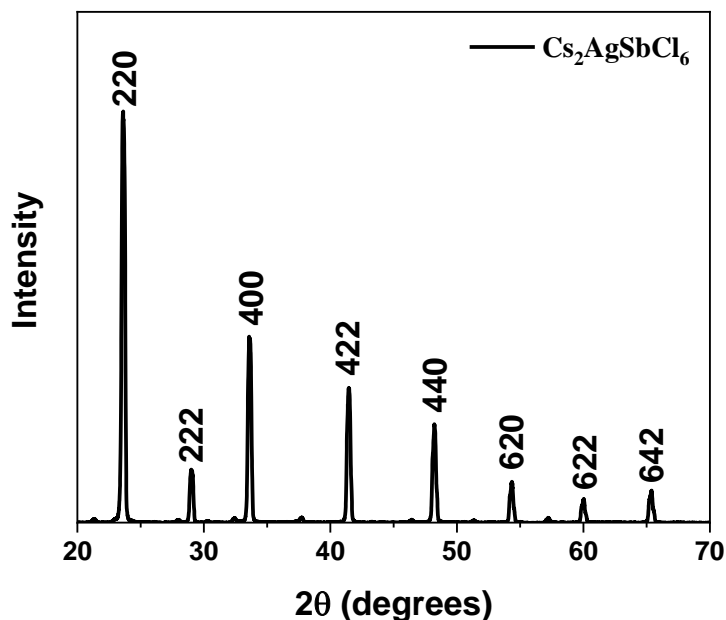
Figure 28. PXRD pattern of $Cs_2AgSbCl_6$ synthesized through acid-mediated solution-phase synthetic route.

The absorption spectra of $Cs_2AgSbCl_6$ shows an indirect bandgap of 2.53 eV whereas $Cs_2Ag_xCu_{(1-x)}SbCl_6$ (x = 0.25, 0.5, 0.75) intermediates show bandgaps ranging from 2.03-2.40 eV. [81,83] The bandgap values of the intermediates obtained from the Tauc plots are listed in Table 3 indicates a decrease in the bandgap with the increment of copper concentration. The absorption spectra and bandgap details of $Cs_2AgSbCl_6$ and the intermediates are obtained from Parth Raval's thesis.

Table 3. Bandgaps of $Cs_2Ag_xCu_{(1-x)}SbCl_6$ (x = 0.25, 0.5, 0.75) intermediates obtained from the Tauc plots.

Intermediates	Bandgap
$Cs_2Ag_{0.75}Cu_{0.25}SbCl_6$	2.40
$Cs_2Ag_{0.50}Cu_{0.50}SbCl_6$	2.31
$Cs_2Ag_{0.25}Cu_{0.75}SbCl_6$	2.03

The PXRD patterns for the intermediates show a small shift in the peaks which is observed due to the change in lattice parameters because of the difference in the concentration of silver and copper in the lattice. The PXRD pattern of $Cs_2Ag_xCu_{(1-x)}SbCl_6$ intermediates along with peak shift is shown in Figure 29.
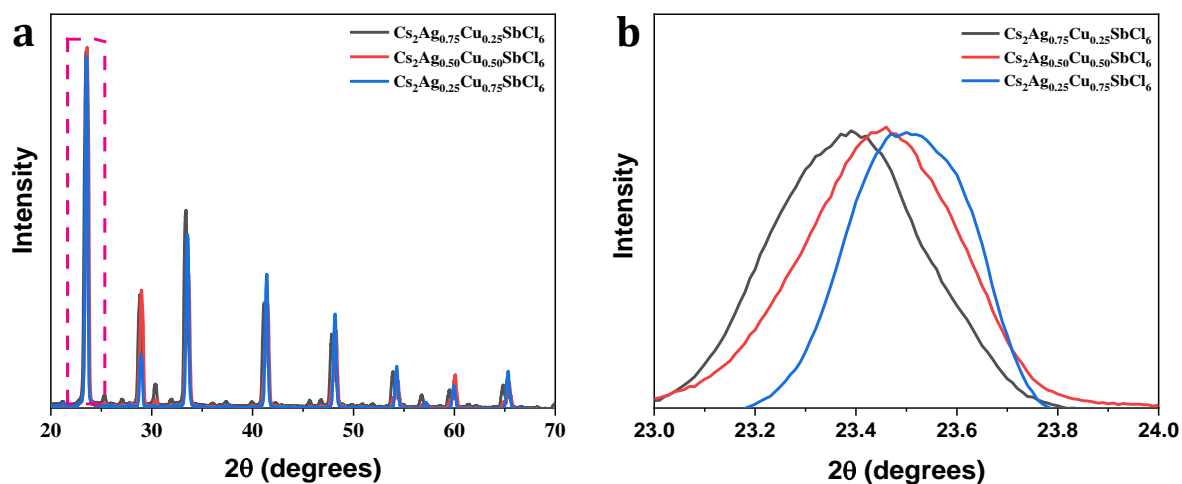
Figure 29. PXRD pattern of (a) $Cs_2Ag_xCu_{(1-x)}SbCl_6$ (x = 0.25, 0.5, 0.75) intermediates and the peak shift corresponding to (220) plane.

As copper (0.77 Å) has a lower ionic radius than silver (1.29 Å), the incorporation of copper into the lattice decreases the lattice parameter. Since the lattice parameter is inversely proportional to the diffraction angle (from Bragg's equation), the peaks will be shifted toward a higher 2θ value with the increment of copper concentration.

$Cs_2AgSbCl_6$ and $Cs_2Ag_xCu_{(1-x)}SbCl_6$ (x = 0.25, 0.5, 0.75) intermediates were synthesized using acid-mediated solution-phase synthesis. Figure 30 shows the FESEM images of $Cs_2AgSbCl_6$ indicating the formation of octahedral shaped polycrystals of size 5.6 μm.
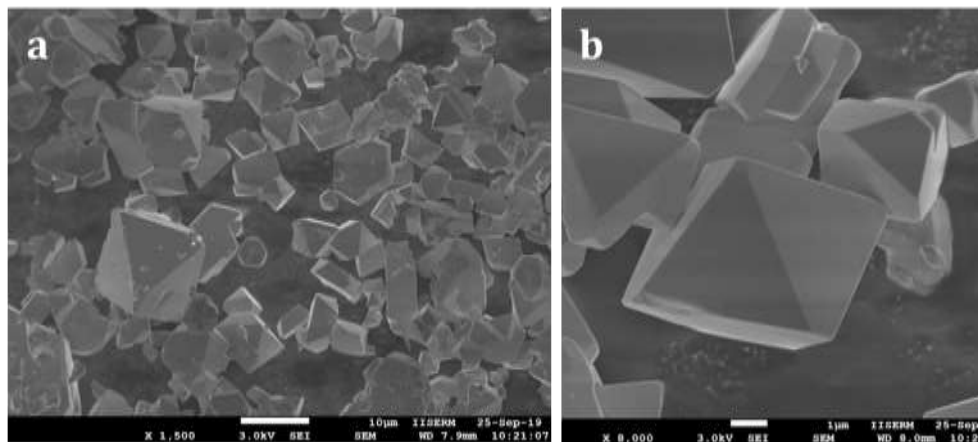
Figure 30. FESEM images of $Cs_2AgSbCl_6$ obtained through acid-mediated solution-phase synthesis at (a) low and (b) high magnification.

Double perovskites are currently explored for their application in photocatalysis. Here, the photocatalytic property of $Cs_2AgSbCl_6$ and $Cs_2Ag_xCu_{(1-x)}SbCl_6$ (x = 0.25, 0.5, 0.75) intermediates has been investigated. For that, $Cs_2AgSbCl_6$ and the intermediate $Cs_2Ag_xCu_{(1-x)}SbCl_6$ (x = 0.25, 0.5, 0.75) were synthesized using acid-mediated solution-phase synthesis. The photocatalytic reactions under sunlight were carried out using the synthesized photocatalysts and evaluated the photocatalytic activity by studying the MB dye degradation. The dye degradation under sunlight in the presence of photocatalysts with increasing irradiation time has been monitored.

MB absorbs light in the visible region with absorption peaks at ~669 and ~605 nm. The degradation of MB dye using $Cs_2AgSbCl_6$ was almost (~96%) completed within 3 hours indicating that $Cs_2AgSbCl_6$ is efficient for photocatalytic reactions. Figure 31 shows the UV-Vis spectra of the MB dye degradation under different irradiation times using different photocatalysts.

From the data it is clear that $Cs_2AgSbCl_6$ show superior activity for MB dye degradation whereas $Cs_2Ag_xCu_{(1-x)}SbCl_6$ (x = 0.25, 0.5, 0.75) intermediates show reduced activity which decreases significantly with increasing the copper concentration.
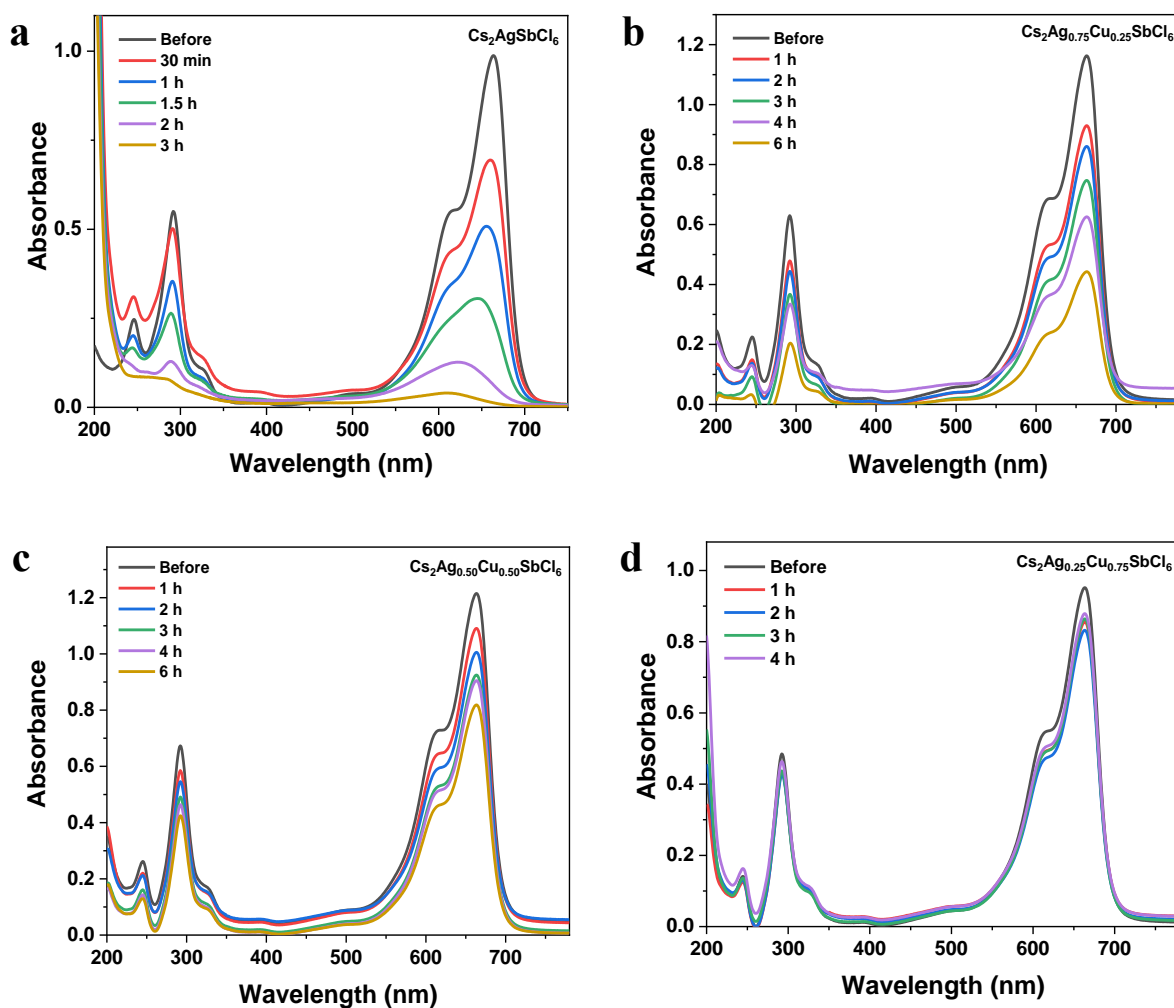
Figure 31. UV-Vis spectra for MB dye degradation under different irradiation time with (a) $Cs_2AgSbCl_6$ and (b, c and d) $Cs_2Ag_xCu_{(1-x)}SbCl_6$ (x = 0.25, 0.5, 0.75) intermediates as photocatalyst.

The photodegradation kinetics of the dye was studied from the pseudo-first-order kinetic rate constants for the dye degradation reaction with each photocatalyst under different irradiation times (Figure 32). The rate constant for the degradation reaction was obtained from the slope of the pseudo-first-order kinetic plot ($ln \frac{C_t}{C_0}$ vs Time). The apparent kinetic rate constant (K_{app}) for the degradation reaction can be calculated from the equation given below[84,85].

$$R = \frac{dC}{dt} = K_{app} . C$$

$$ln \frac{C_t}{C_0} = K_{app} . t$$

where R is the reaction rate, t is the reaction time, K_{app} is the apparent kinetic rate constant, C_0 is the initial concentration of the dye solution, and C_t is the concentration of the dye solution at time t.

From the kinetic plots, it is clear that the decomposition of MB dye using $Cs_2AgSbCl_6$ photocatalyst has shown a higher rate (~10 times higher) compared to other intermediates indicating that $Cs_2AgSbCl_6$ can be used as an effective photocatalyst for MB dye degradation.
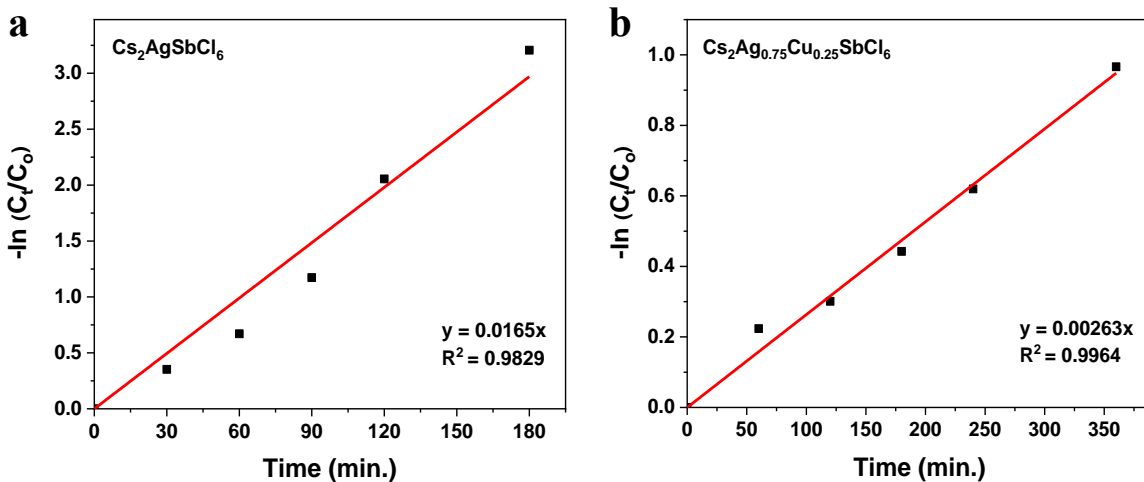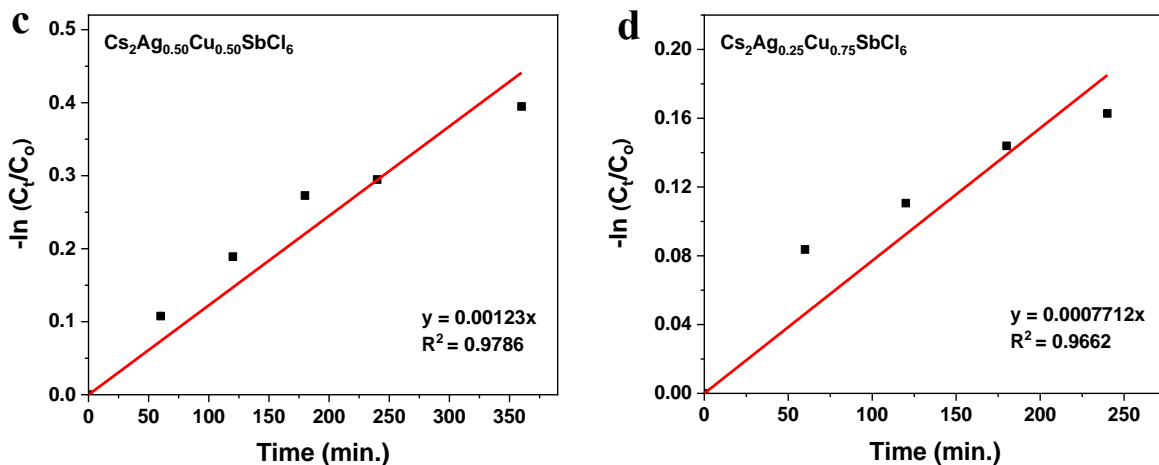
Figure 32. Pseudo-first-order kinetic plots for MB dye degradation under different irradiation time with (a) $Cs_2AgSbCl_6$ and (b, c and d) $Cs_2Ag_xCu_{(1-x)}SbCl_6$ (x = 0.25, 0.5, 0.75) intermediates as photocatalyst.

Table 4. Apparent first-order kinetic rate constant for MB dye degradation using different photocatalysts.

Photocatalyst	K_{app} (min^{-1})
$Cs_2AgSbCl_6$	1.65×10^{-2}
$Cs_2Ag_{0.75}Cu_{0.25}SbCl_6$	2.63×10^{-3}
$Cs_2Ag_{0.50}Cu_{0.50}SbCl_6$	1.23×10^{-3}
$Cs_2Ag_{0.25}Cu_{0.75}SbCl_6$	7.71×10^{-4}

The degradation of MB dye without sunlight and photocatalyst was also evaluated. Even though the dye degrades under sunlight without photocatalyst, the rate of degradation is much slower compared to the one in the presence of photocatalyst. The dye degradation without sunlight was found to be negligible. Figure 33 shows the UV-Vis spectra of the MB dye degradation in the absence of sunlight and photocatalyst.
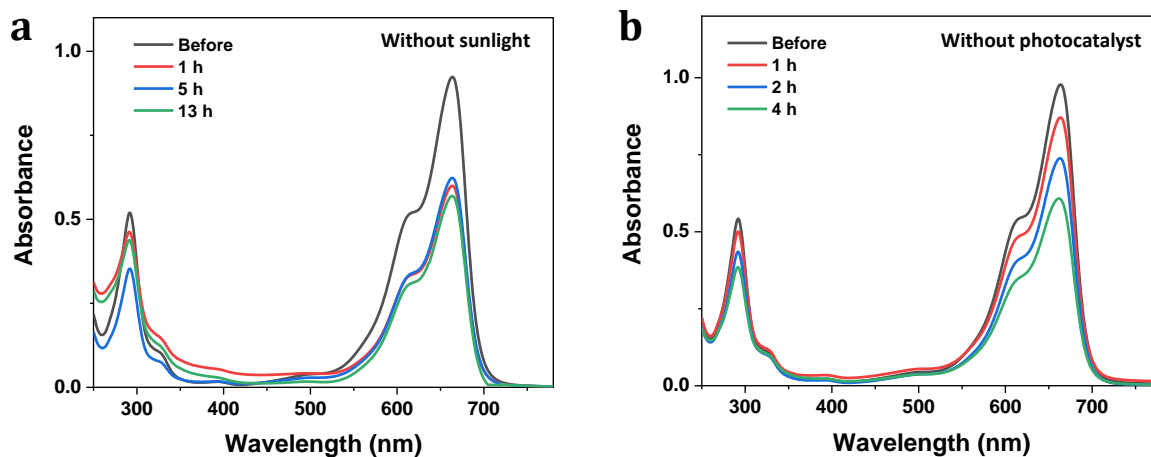
Figure 33. UV-Vis spectra for MB dye degradation under different irradiation time (a) without sunlight and (b) without photocatalyst.

The reusability of these photocatalysts was assessed by carrying out multiple reactions with the same photocatalyst. The observed degradation rate for each cycle is shown in Figure 34 and the corresponding values are reported in Table 5. After two cycles of photodegradation, the photocatalytic activity of $Cs_2AgSbCl_6$ had remarkably reduced. The reduced activity may be attributed to the decreased stability and photocatalytic efficiency of $Cs_2AgSbCl_6$ due to the dissolution of the photocatalyst in water.
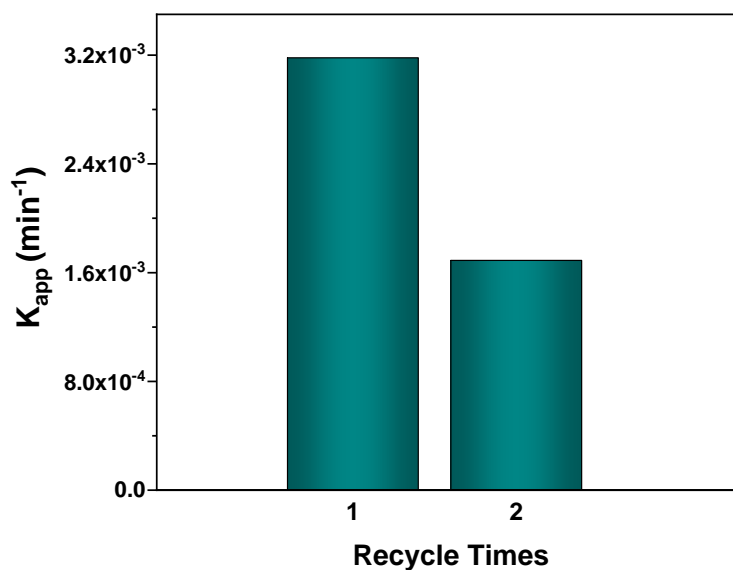
Figure 34. Reusability of $Cs_2AgSbCl_6$ photocatalyst for MB dye degradation reaction.

Table 5. Apparent first-order kinetic rate constant for MB dye degradation under different recycle times using $Cs_2AgSbCl_6$ photocatalyst.

Recycle Times	K_{app} (min^{-1})
1	3.18×10^{-3}
2	1.69×10^{-3}

Further studies include the understanding of the mechanism and confirming the activity of the photocatalyst through various photocatalytic reactions. As already discussed, the major active species involved in a photocatalytic process are the VB holes, CB electrons, hydroxide radicals ($\dot{O}H$), and superoxide radicals ($\dot{O}_2^-$). To evaluate the mechanism of MB dye degradation, it is necessary to identify which active species are mainly involved in the photocatalytic reaction. For that, various active species scavengers are used in the reaction such that a reduction in the photodegradation rate is observed.

If the photodegradation is significantly reduced after the addition of free-radical scavengers such as TEMPO and DMPO, the major species involved in the process are identified to be $\dot{O}_2^-$ or $\dot{O}H$ radical which can be proved by spin-trapping ESR measurements.[66] The ESR spectra will show a six-line spectrum identified according to the ^{1}H hyperfine coupling constants of the scavengers. DMPO traps hydroxyl radical and superoxide, forming adducts with $\dot{O}H$ or $\dot{O}OH$. All H atoms and hydrated electrons would react with DMPO, yielding DMPO-H. With $\dot{O}H$ radical, the characteristic quadruple peaks of the DMPO–$\dot{O}H$ adducts will be detected.

Other scavengers include the silver ion (Ag$^+$) which decreases the reaction rate by trapping the CB electrons that block the generation of $\dot{O}_2^-$ radicals. Similarly, if $\dot{O}H$ radicals are involved in the process, a reduced degradation rate will be observed in the presence of DMSO or SO that trap the holes restricting the conversion to $\dot{O}H$ radicals.[56] Yang *et al.* reported that the use of KI suppresses the VB holes and thereby the $\dot{O}H$ radicals showing a reduced photodegradation.[86] Other reports mentioned the use of ethylenediaminetetraacetic acid (EDTA) and benzoquinone as H$^+$ and $\dot{O}_2^-$ scavengers inhibiting degradation by up to 26% and

37% respectively. Also, the use of 2-propanol reduced the degradation rate up to 75%.[87] Thus, in this work, the major active species involved in the photodegradation reaction can be identified by using different possible scavengers, and the species corresponding to the scavenger that significantly reduces the degradation reaction rate will be considered as the key initiator of the reaction.

Conclusion

2D layered $Cs_4CuSb_2Cl_{12}$ and 3D $Cs_2AgSbCl_6$ were successfully synthesized *via* hot injection method and acid-mediated solution-phase synthetic route respectively. $Cs_4CuSb_2Cl_{12}$ NCs of size around 4 nm are found to be stable under air, heat, and moisture. The Tauc plot revealed that the NCs possess a bandgap within 1.3-1.6 eV and can be used as a photovoltaic material. The synthesis is also scalable and the NCs have a thickness of a single unit cell confirmed by AFM study. Synthesis of bromine analog of $Cs_4CuSb_2Cl_{12}$ was also attempted but no formation of $Cs_4CuSb_2Br_{12}$ was observed due to the instability of $[CuBr_6]$ octahedra towards its formation. $Cs_2AgSbCl_6$ and intermediate $Cs_2Ag_xCu_{(1-x)}SbCl_6$ (x = 0.25, 0.5, 0.75) show bandgap values decreasing from 2.53 to 2.03 with the increment of copper concentration which is confirmed by the peak shift observed from the XRD data. Photocatalytic reactions carried out using $Cs_2AgSbCl_6$ and its Cu-doped intermediates as photocatalysts revealed that $Cs_2AgSbCl_6$ shows excellent photocatalytic activity for MB dye degradation than its intermediates.

Future Outlook

Cs$_4$CuSb$_2$Cl$_{12}$ NCs exhibit low bandgap and high stability which can be utilized in single-junction solar cells. Also, the bandgap of the NCs can be tuned by doping with other metal ions to improve the PCE of the device and for a better understanding of their properties.[88] These halide double perovskites open the possibility of developing new layered materials with attractive and tunable properties for photovoltaics and optoelectronics in the future.

As Cs$_2$AgSbCl$_6$ double perovskite has shown excellent photocatalytic efficiency for MB dye degradation, its activity towards other photocatalytic reactions can also be studied. Further efforts can be made to enhance the degradation rate by doping other metal ions to reduce the electron-hole recombination and bandgap of the material or by improving the synthetic method to yield highly stable perovskite photocatalysts with better properties.

References

(1)   Mao, L.; Teicher, S. M. L.; Stoumpos, C. C.; Kennard, R. M.; Decrescent, R. A.; Wu, G.; Schuller, J. A.; Chabinyc, M. L.; Cheetham, A. K.; Seshadri, R. Chemical and Structural Diversity of Hybrid Layered Double Perovskite Halides. *J. Am. Chem. Soc.* **2019**, *141* (48), 19099–19109.

(2)   Nada F. Atta, A. G. and E. H. E.-A. Perovskite Nanomaterials – Synthesis, Characterization, and Applications. *Perovskite Mater. - Synth. Characterisation, Prop. Appl.* **2016**, 107–151.

(3)   Jayatissa, Z. S. and A. H. Perovskites-Based Solar Cells : A Review of Recent Progress , Materials and Processing Methods. **2018**, *11* (729), 1–34.

(4)   Yi, Z.; Ladi, N. H.; Shai, X.; Li, H.; Shen, Y.; Wang, M. Will Organic-Inorganic Hybrid Halide Lead Perovskites Be Eliminated from Optoelectronic Applications? *Nanoscale Adv.* **2019**, *1* (4), 1276–1289.

(5)   Dai, J.; Ma, L.; Ju, M.; Huang, J.; Zeng, X. C. In- and Ga-Based Inorganic Double Perovskites with Direct Bandgaps for Photovoltaic Applications. *Phys. Chem. Chem. Phys.* **2017**, *19* (32), 21691–21695.

(6)   Ananthakumar, S.; Moorthy Babu, S. Progress on Synthesis and Applications of Hybrid Perovskite Semiconductor Nanomaterials—A Review. *Synth. Met.* **2018**, *246*, 64–95.

(7)   Hossain, A.; Bandyopadhyay, P.; Roy, S. An Overview of Double Perovskites $A_2B'B''O_6$ with Small Ions at A Site: Synthesis, Structure and Magnetic Properties. *J. Alloys Compd.* **2018**, *740*, 414–427.

(8)   Assirey, E. A. R. Perovskite Synthesis, Properties and Their Related Biochemical and Industrial Application. *Saudi Pharm. J.* **2019**, *27* (6), 817–829.

(9)   Vidyasagar, C. C.; Muñoz Flores, B. M.; Jiménez Pérez, V. M. Recent Advances in Synthesis and Properties of Hybrid Halide Perovskites for Photovoltaics. *Nano-Micro Lett.* **2018**, *10* (4), 1–34.

(10)   Shamsi, J.; Urban, A. S.; Imran, M.; De Trizio, L.; Manna, L. Metal Halide Perovskite

Nanocrystals: Synthesis, Post-Synthesis Modifications, and Their Optical Properties. *Chem. Rev.* **2019**, *119* (5), 3296–3348.

(11)   Talapin, D. V; Lee, J.; Kovalenko, M. V; Shevchenko, E. V. Prospects of Colloidal Nanocrystals for Electronic and Optoelectronic Applications. *Chem. Rev.* **2010**, *110* (1), 389–458.

(12)   Kulkarni, S. A.; Mhaisalkar, S. G.; Mathews, N.; Boix, P. P. Perovskite Nanoparticles: Synthesis, Properties, and Novel Applications in Photovoltaics and LEDs. *Small Methods* **2019**, *3* (1), 1–16.

(13)   Antony K. J., I.; Jana, D. Stable Mn-Doped $CsPbCl_3$ Nanocrystals inside Mesoporous Alumina Films for Display and Catalytic Applications. *ACS Appl. Nano Mater.* **2020**, *3* (3), 2941–2951.

(14)   Takhellambam, D.; Meena, T. R.; Jana, D. Room Temperature Synthesis of Blue and Green Emitting $CsPbBr_3$ Perovskite Nanocrystals Confined in Mesoporous Alumina Film. *Chem. Commun.* **2019**, *55* (33), 4785–4788.

(15)   Li, Y.; Zhang, X.; Huang, H.; Kershaw, S. V; Rogach, A. L. Advances in Metal Halide Perovskite Nanocrystals: Synthetic Strategies, Growth Mechanisms, and Optoelectronic Applications. *Mater. Today* **2020**, *32*, 204–221.

(16)   Rosales, B. A.; Wei, L.; Vela, J. Synthesis and Mixing of Complex Halide Perovskites by Solvent-Free Solid-State Methods. *J. Solid State Chem.* **2019**, *271*, 206–215.

(17)   Jena, A. K.; Kulkarni, A.; Miyasaka, T. Halide Perovskite Photovoltaics: Background, Status, and Future Prospects. *Chem. Rev.* **2019**, *119* (5), 3036–3103.

(18)   Koliogiorgos, A.; Baskoutas, S.; Galanakis, I. Electronic and Gap Properties of Lead-Free Perfect and Mixed Hybrid Halide Perovskites : An Ab-Initio Study. *Comput. Mater. Sci.* **2017**, *138*, 92–98.

(19)   Huang, H.; Bodnarchuk, M. I.; Kershaw, S. V.; Kovalenko, M. V.; Rogach, A. L. Lead Halide Perovskite Nanocrystals in the Research Spotlight: Stability and Defect Tolerance. *ACS Energy Lett.* **2017**, *2* (9), 2071–2083.

(20)   Kang, J.; Wang, L. W. High Defect Tolerance in Lead Halide Perovskite $CsPbBr_3$. *J.*

Phys. Chem. Lett. **2017**, *8* (2), 489–493.

(21)   Huang, J.; Yuan, Y.; Shao, Y.; Yan, Y. Understanding the Physical Properties of Hybrid Perovskites for Photovoltaic Applications. *Nat. Rev. Mater.* **2017**, *2*, 1–19.

(22)   Andreani, L. C.; Bozzola, A.; Kowalczewski, P.; Liscidini, M.; Redorici, L. Silicon Solar Cells: Toward the Efficiency Limits. *Adv. Phys. X* **2019**, *4* (1), 125–148.

(23)   Zhao, X. G.; Yang, D.; Ren, J. C.; Sun, Y.; Xiao, Z.; Zhang, L. Rational Design of Halide Double Perovskites for Optoelectronic Applications. *Joule* **2018**, *2* (9), 1662–1673.

(24)   Protesescu, L.; Yakunin, S.; Bodnarchuk, M. I.; Krieg, F.; Caputo, R.; Hendon, C. H.; Yang, R. X.; Walsh, A.; Kovalenko, M. V. Nanocrystals of Cesium Lead Halide Perovskites (CsPbX$_3$, X = Cl, Br, and I): Novel Optoelectronic Materials Showing Bright Emission with Wide Color Gamut. *Nano Lett.* **2015**, *15* (6), 3692–3696.

(25)   Chu, L.; Ahmad, W.; Liu, W.; Yang, J.; Zhang, R.; Sun, Y. Lead - Free Halide Double Perovskite Materials : A New Superstar Toward Green and Stable Optoelectronic Applications. *Nano-Micro Lett.* **2019**, *11* (16), 1–18.

(26)   Filip, M. R.; Hillman, S.; Haghighirad, A. A.; Snaith, H. J.; Giustino, F. Band Gaps of the Lead-Free Halide Double Perovskites Cs$_2$BiAgCl$_6$ and Cs$_2$BiAgBr$_6$ from Theory and Experiment. *J. Phys. Chem. Lett.* **2016**, *7*, 2579–2585.

(27)   Ball, J. M.; Petrozza, A. Defects in Perovskite-Halides and Their Effects in Solar Cells. *Nat. Energy* **2016**, *1* (11), 1–13.

(28)   Fu, Y.; Zhu, H.; Chen, J.; Hautzinger, M. P.; Zhu, X. Y.; Jin, S. Metal Halide Perovskite Nanostructures for Optoelectronic Applications and the Study of Physical Properties. *Nat. Rev. Mater.* **2019**, *4* (3), 169–188.

(29)   Lou, S.; Xuan, T.; Wang, J. Stability: A Desiderated Problem for the Lead Halide Perovskites. *Opt. Mater. X* **2019**, *1*, 1–17.

(30)   Chen, X.; Wang, Z. Investigating Chemical and Structural Instabilities of Lead Halide Perovskite Induced by Electron Beam Irradiation. *Micron* **2019**, *116*, 73–79.

(31)   Wang, K.; Yang, D.; Wu, C.; Sanghadasa, M.; Priya, S. Recent Progress in Fundamental

Understanding of Halide Perovskite Semiconductors. *Prog. Mater. Sci.* **2019**, *106*, 100580.

(32) Khalfin, S.; Bekenstein, Y. Advances in Lead-Free Double Perovskite Nanocrystals, Engineering Band-Gaps and Enhancing Stability through Composition Tunability. **2019**, *11*, 8665–8679.

(33) Ravi, V. K.; Singhal, N.; Nag, A. Initiation and Future Prospects of Colloidal Metal Halide Double-Perovskite Nanocrystals: Cs_2AgBiX_6 (X = Cl, Br, I). *J. Mater. Chem. A* **2018**, *6* (44), 21666–21675.

(34) Igbari, F.; Wang, Z. K.; Liao, L. S. Progress of Lead-Free Halide Double Perovskites. *Adv. Energy Mater.* **2019**, *9* (12), 1–32.

(35) Chatterjee, S.; Pal, A. J. Influence of Metal Substitution on Hybrid Halide Perovskites: Towards Lead-Free Perovskite Solar Cells. *J. Mater. Chem. A* **2018**, *6* (9), 3793–3823.

(36) Fu, H. Review of Lead-Free Halide Perovskites as Light-Absorbers for Photovoltaic Applications: From Materials to Solar Cells. *Sol. Energy Mater. Sol. Cells* **2019**, *193*, 107–132.

(37) Meyer, E.; Mutukwa, D.; Zingwe, N.; Taziwa, R. Lead-Free Halide Double Perovskites: A Review of the Structural, Optical, and Stability Properties as Well as Their Viability to Replace Lead Halide Perovskites. *Metals (Basel).* **2018**, *8* (667), 1–16.

(38) Volonakis, G.; Filip, M. R.; Haghighirad, A. A.; Sakai, N.; Wenger, B.; Snaith, H. J.; Giustino, F. Lead-Free Halide Double Perovskites via Heterovalent Substitution of Noble Metals. *J. Phys. Chem. Lett.* **2016**, *7* (7), 1254–1259.

(39) Zhang, P.; Yang, J.; Wei, S. H. Manipulation of Cation Combinations and Configurations of Halide Double Perovskites for Solar Cell Absorbers. *J. Mater. Chem. A* **2018**, *6* (4), 1809–1815.

(40) Lan, C.; Zhao, S.; Luo, J.; Fan, P. First-Principles Study of Anion Diffusion in Lead-Free Halide Double Perovskites. *Phys. Chem. Chem. Phys.* **2018**, *20* (37), 24339–24344.

(41) Wang, R.; Wang, J.; Tan, S.; Duan, Y.; Wang, Z. K.; Yang, Y. Opportunities and Challenges of Lead-Free Perovskite Optoelectronic Devices. *Trends Chem.* **2019**, *1* (4),

368–379.

(42)   Creutz, S. E.; Crites, E. N.; Siena, M. C. De; Gamelin, D. R. Colloidal Nanocrystals of
         Lead-Free Double-Perovskite (Elpasolite) Semiconductors: Synthesis and Anion
         Exchange To Access New Materials. *Nano Lett.* **2018**, *18*, 1118–1123.

(43)   Hoefler, S. F.; Trimmel, G.; Rath, T. Progress on Lead-Free Metal Halide Perovskites
         for Photovoltaic Applications: A Review. *Monatshefte fur Chemie* **2017**, *148* (5), 795–
         826.

(44)   Creutz, S. E.; Crites, E. N.; De Siena, M. C.; Gamelin, D. R. Colloidal Nanocrystals of
         Lead-Free Double-Perovskite (Elpasolite) Semiconductors: Synthesis and Anion
         Exchange to Access New Materials. *Nano Lett.* **2018**, *18* (2), 1118–1123.

(45)   Xu, L.; Yuan, S.; Zeng, H.; Song, J. A Comprehensive Review of Doping in Perovskite
         Nanocrystals/Quantum Dots: Evolution of Structure, Electronics, Optics, and Light-
         Emitting Diodes. *Mater. Today Nano* **2019**, *6*, 1–15.

(46)   Connor, B. A.; Leppert, L.; Smith, M. D.; Neaton, B.; Karunadasa, H. I. Layered Halide
         Double Perovskites: Dimensional Reduction of $Cs_2AgBiBr_6$. *J. Am. Chem. Soc.* **2018**,
         140, 5325–5240.

(47)   Liu, Y.; Li, F.; Yao, F.; He, Z.; Liu, S.; Xu, L.; Han, X. Synthesis , Structure and
         Photoluminescence Properties of 2D Organic – Inorganic Hybrid Perovskites. *Appl. Sci.*
         2019, *9* (5211), 1–14.

(48)   Li, Y.; Yang, T.; Xu, Z.; Liu, X.; Huang, X.; Han, S.; Liu, Y.; Li, M.; Luo, J.; Sun, Z.
         Dimensional Reduction of $Cs_2AgBiBr_6$: A 2D Hybrid Double Perovskite with Strong
         Polarization Sensitivity. *Angew. Chemie* **2020**, *132* (9), 3457–3461.

(49)   Wang, X. D.; Miao, N. H.; Liao, J. F.; Li, W. Q.; Xie, Y.; Chen, J.; Sun, Z. M.; Chen,
         H. Y.; Kuang, D. Bin. The Top-down Synthesis of Single-Layered $Cs_4CuSb_2Cl_{12}$ Halide
         Perovskite Nanocrystals for Photoelectrochemical Application. *Nanoscale* **2019**, *11*
         (12), 5180–5187.

(50)   Zhang, Y.; Yin, J.; Parida, M. R.; Ahmed, G. H.; Pan, J.; Bakr, O. M.; Mohammed, O.
         F. Direct-Indirect Nature of the Bandgap in Lead-Free Perovskite Nanocrystals. *J. Phys.
         Chem. Lett.* **2017**, *8*, 3173–3177.

(51) Pradhan, B.; Kumar, G. S.; Sain, S.; Dalui, A.; Ghorai, U. K.; Pradhan, S. K.; Acharya, S. Size Tunable Cesium Antimony Chloride Perovskite Nanowires and Nanorods. *Chem. Mater.* **2018**, *30* (6), 2135–2142.

(52) Nie, K.; Yang, H.; Gao, Z.; Wu, J. Fe-Modified Perovskite-Type $NaMgF_3$ Photocatalyst: Synthesis and Photocatalytic Properties. *Mater. Sci. Semicond. Process.* **2018**, *83*, 12–17.

(53) Halder, S.; Sheikh, M. S.; Maity, R.; Ghosh, B.; Sinha, T. P. Investigating the Optical, Photosensitivity and Photocatalytic Properties of Double Perovskites A_2LuTaO_6 (A = Ba, Sr): A Combined Experimental and Density Functional Theory Study. *Ceram. Int.* **2019**, *45* (12), 15496–15504.

(54) Nagarajan, S.; Skillen, N. C.; Fina, F.; Zhang, G.; Randorn, C.; Lawton, L. A.; Irvine, J. T. S.; Robertson, P. K. J. Comparative Assessment of Visible Light and UV Active Photocatalysts by Hydroxyl Radical Quantification. *J. Photochem. Photobiol. A Chem.* **2017**, *334*, 13–19.

(55) Ajmal, A.; Majeed, I.; Malik, R. N.; Idriss, H.; Nadeem, M. A. Principles and Mechanisms of Photocatalytic Dye Degradation on TiO_2 Based Photocatalysts: A Comparative Overview. *RSC Adv.* **2014**, *4* (70), 37003–37026.

(56) Da Silva, L. F.; Lopes, O. F.; De Mendonça, V. R.; Carvalho, K. T. G.; Longo, E.; Ribeiro, C.; Mastelaro, V. R. An Understanding of the Photocatalytic Properties and Pollutant Degradation Mechanism of $SrTiO_3$ Nanoparticles. *Photochem. Photobiol.* **2016**, *92* (3), 371–378.

(57) Kong, J.; Yang, T.; Rui, Z.; Ji, H. Perovskite-Based Photocatalysts for Organic Contaminants Removal: Current Status and Future Perspectives. *Catal. Today* **2019**, *327*, 47–63.

(58) Yang, C.; Zhang, M.; Dong, W.; Cui, G.; Ren, Z.; Wang, W. Highly Efficient Photocatalytic Degradation of Methylene Blue by $PoPD/TiO_2$ Nanocomposite. *PLoS One* **2017**, *12* (3), 1–16.

(59) Kanhere, P.; Chen, Z. A Review on Visible Light Active Perovskite-Based Photocatalysts. *Molecules* **2014**, *19* (12), 19995–20022.

(60) Teh, Y. W.; Chee, M. K. T.; Kong, X. Y.; Yong, S. T.; Chai, S. P. An Insight into Perovskite-Based Photocatalysts for Artificial Photosynthesis. *Sustain. Energy Fuels* **2020**, *4* (3), 973–984.

(61) Wang, W.; Tadé, M. O.; Shao, Z. Research Progress of Perovskite Materials in Photocatalysis- and Photovoltaics-Related Energy Conversion and Environmental Treatment. *Chem. Soc. Rev.* **2015**, *44* (15), 5371–5408.

(62) Zlotnik, S.; Tobaldi, D. M.; Seabra, P.; Labrincha, J. A.; Vilarinho, P. M. Alkali Niobate and Tantalate Perovskites as Alternative Photocatalysts. *ChemPhysChem* **2016**, *17* (21), 3570–3575.

(63) Zhu, X.; Lin, Y.; Sun, Y.; Beard, M. C.; Yan, Y. Lead-Halide Perovskites for Photocatalytic α-Alkylation of Aldehydes. *J. Am. Chem. Soc.* **2019**, *141* (2), 733–738.

(64) Zhu, X.; Lin, Y.; San Martin, J.; Sun, Y.; Zhu, D.; Yan, Y. Lead Halide Perovskites for Photocatalytic Organic Synthesis. *Nat. Commun.* **2019**, *10* (1), 1–10.

(65) Xu, X.; Zhong, Y.; Shao, Z. Double Perovskites in Catalysis, Electrocatalysis, and Photo(Electro)Catalysis. *Trends Chem.* **2019**, *1* (4), 410–424.

(66) Zhang, Z.; Liang, Y.; Huang, H.; Liu, X.; Li, Q.; Chen, L.; Xu, D. Stable and Highly Efficient Photocatalysis with Lead-Free Double-Perovskite of $Cs_2AgBiBr_6$. *Angew. Chemie - Int. Ed.* **2019**, *58* (22), 7263–7267.

(67) Yin, W. J.; Weng, B.; Ge, J.; Sun, Q.; Li, Z.; Yan, Y. Oxide Perovskites, Double Perovskites and Derivatives for Electrocatalysis, Photocatalysis, and Photovoltaics. *Energy Environ. Sci.* **2019**, *12* (2), 442–462.

(68) Huynh, K. A.; Nguyen, D. L. T.; Nguyen, V. H.; Vo, D. V. N.; Trinh, Q. T.; Nguyen, T. P.; Kim, S. Y.; Le, Q. Van. Halide Perovskite Photocatalysis: Progress and Perspectives. *J. Chem. Technol. Biotechnol.* **2020**.

(69) Cai, Y.; Xie, W.; Teng, Y. T.; Harikesh, P. C.; Ghosh, B.; Huck, P.; Persson, K. A.; Mathews, N.; Mhaisalkar, S. G.; Sherburne, M.; Asta, M. High-Throughput Computational Study of Halide Double Perovskite Inorganic Compounds. *Chem. Mater.* **2019**, *31* (15), 5392–5401.

(70) Filip, M. R.; Liu, X.; Miglio, A.; Hautier, G.; Giustino, F. Phase Diagrams and Stability of Lead-Free Halide Double Perovskites $Cs_2BB'X_6$: B = Sb and Bi, B' = Cu, Ag, and Au, and X = Cl, Br, and I. *J. Phys. Chem. C* **2018**, *122* (1), 158–170.

(71) Xiao, Z.; Du, K. Z.; Meng, W.; Mitzi, D. B.; Yan, Y. Chemical Origin of the Stability Difference between Cu(I)- and Ag(I)-Based Halide Double Perovskites. *Angew. Chemie - Int. Ed.* **2017**, *56* (40), 12107–12111.

(72) Singhal, N.; Chakraborty, R.; Ghosh, P.; Nag, A. Low-Bandgap $Cs_4CuSb_2Cl_{12}$ Layered Double Perovskite: Synthesis, Reversible Thermal Changes, and Magnetic Interaction. *Chem. - An Asian J.* **2018**, *13* (16), 2085–2092.

(73) Brenda Vargas, Estrella Ramos, Enrique Pérez-Gutiérrez, Juan Carlos Alonso, and D. S.-I. Direct Bandgap Copper−Antimony Halide Perovskite. *J. Am. Chem. Soc.* **2017**, *139*, 9116–9119.

(74) Locardi, F.; Cirignano, M.; Baranov, D.; Dang, Z.; Prato, M.; Drago, F.; Ferretti, M.; Pinchetti, V.; Fanciulli, M.; Brovelli, S.; De Trizio, L.; Manna, L. Colloidal Synthesis of Double Perovskite $Cs_2AgInCl_6$ and Mn-Doped $Cs_2AgInCl_6$ Nanocrystals. *J. Am. Chem. Soc.* **2018**, *140* (40), 12989–12995.

(75) Chen, W.; Shi, T.; Du, J.; Zang, Z.; Yao, Z.; Li, M.; Sun, K.; Hu, W.; Leng, Y.; Tang, X. Highly Stable Silica-Wrapped Mn-Doped $CsPbCl_3$ Quantum Dots for Bright White Light-Emitting Devices. *ACS Appl. Mater. Interfaces* **2018**, *10* (50), 43978–43986.

(76) Volonakis, G.; Haghighirad, A. A.; Milot, R. L.; Sio, W. H.; Filip, M. R.; Wenger, B.; Johnston, M. B.; Herz, L. M.; Snaith, H. J.; Giustino, F. $Cs_2InAgCl_6$: A New Lead-Free Halide Double Perovskite with Direct Band Gap. *J. Phys. Chem. Lett.* **2017**, *8*, 772–778.

(77) Iso, Y.; Isobe, T. Review—Synthesis, Luminescent Properties, and Stabilities of Cesium Lead Halide Perovskite Nanocrystals. *ECS J. Solid State Sci. Technol.* **2018**, *7* (1), R3040–R3045.

(78) Huang, H.; Pradhan, B.; Hofkens, J.; Roeffaers, M. B. J.; Steele, J. A. Solar-Driven Metal Halide Perovskite Photocatalysis: Design, Stability, and Performance. *ACS Energy Lett.* **2020**, *5* (4), 1107–1123.

(79) Bhattacharjee, S.; Chaudhary, S. P.; Bhattacharyya, S. Lead-Free Metal Halide

Perovskite Nanocrystals for Photocatalysis in Water. **2019**, No. 2.

(80) Zhou, L.; Xu, Y. F.; Chen, B. X.; Kuang, D. Bin; Su, C. Y. Synthesis and Photocatalytic Application of Stable Lead-Free $Cs_2AgBiBr_6$ Perovskite Nanocrystals. *Small* **2018**, *14* (11), 1–7.

(81) Deng, W.; Deng, Z. Y.; He, J.; Wang, M.; Chen, Z. X.; Wei, S. H.; Feng, H. J. Synthesis of $Cs_2AgSbCl_6$ and Improved Optoelectronic Properties of $Cs_2AgSbCl_6/TiO_2$ Heterostructure Driven by the Interface Effect for Lead-Free Double Perovskites Solar Cells. *Appl. Phys. Lett.* **2017**, *111* (15), 2–7.

(82) Tran, T. T.; Panella, J. R.; Chamorro, J. R.; Morey, J. R.; McQueen, T. M. Designing Indirect-Direct Bandgap Transitions in Double Perovskites. *Mater. Horizons* **2017**, *4* (4), 688–693.

(83) Dahl, J. C.; Osowiecki, W. T.; Cai, Y.; Swabeck, J. K.; Bekenstein, Y.; Asta, M.; Chan, E. M.; Alivisatos, A. P. Probing the Stability and Band Gaps of $Cs_2AgInCl_6$ and $Cs_2AgSbCl_6$ Lead-Free Double Perovskite Nanocrystals. *Chem. Mater.* **2019**, *31* (9), 3134–3143.

(84) Pradeeba, S. J.; Sampath, K. A Comparative Study of Photo-Catalytic Degradation Efficiency of Methylene Blue Dye in Waste Water Using Poly(Azomethine)/ZnO Nanocomposite and Poly(Azomethine)/TiO_2 Nanocomposite. *J. Ovonic Res.* **2018**, *14* (3), 243–259.

(85) Jouali, A.; Salhi, A.; Aguedach, A.; Aarfane, A.; Ghazzaf, H.; Lhadi, E. K.; El krati, M.; Tahiri, S. Photo-Catalytic Degradation of Methylene Blue and Reactive Blue 21 Dyes in Dynamic Mode Using TiO_2 Particles Immobilized on Cellulosic Fibers. *J. Photochem. Photobiol. A Chem.* **2019**, *383*, 1–8.

(86) Kuang, L.; Zhao, Y.; Zhang, W.; Ge, S. Roles of Reactive Oxygen Species and Holes in the Photodegradation of Cationic and Anionic Dyes by TiO_2 under UV Irradiation. *J. Environ. Eng. (United States)* **2016**, *142* (2), 1–6.

(87) Bhuvaneswari, K.; Palanisamy, G.; Pazhanivel, T.; Bharathi, G.; Nataraj, D. Photocatalytic Performance on Visible Light Induced ZnS QDs-MgAl Layered Double Hydroxides Hybrids for Methylene Blue Dye Degradation. *ChemistrySelect* **2018**, *3*

(47), 13419–13426.

(88)   Liu, Y.; Zhang, L.; Wang, M.; Zhong, Y.; Huang, M.; Long, Y.; Zhu, H. Bandgap-Tunable Double-Perovskite Thin Films by Solution Processing. *Mater. Today* **2019**, *28*, 25–30.